



**TURUN
YLIOPISTO**
UNIVERSITY
OF TURKU

NOVEL BONE SPECT-CT METHODS

Optimization and Validation
for Imaging Bone Metastases

Samuli Arvola



**TURUN
YLIOPISTO**
UNIVERSITY
OF TURKU

NOVEL BONE SPECT-CT METHODS

Optimization and Validation for Imaging Bone
Metastases

Samuli Arvola

University of Turku

Faculty of Medicine
Institute of Biomedicine
Medical Physics and Engineering
Doctoral Programme in Clinical Research

Supervised by

Adjunct Professor Tommi Noponen
Department of Nuclear Medicine
Turku University Hospital
Turku, Finland

Adjunct Professor Marko Seppänen
Department of Nuclear Medicine
Turku PET Centre
Turku University Hospital
Turku, Finland

Reviewed by

Adjunct Professor Tiina Laitinen
Department of Nuclear Medicine
Kuopio University Hospital
Kuopio, Finland

Professor John Dickson
Institute of Nuclear Medicine
University College London Hospital
London, United Kingdom

Opponent

Adjunct Professor Outi Sipilä
Department of Nuclear Medicine
Helsinki University Central Hospital
Helsinki, Finland

The originality of this publication has been checked in accordance with the University of Turku quality assurance system using the Turnitin OriginalityCheck service.

Cover Image: Midjourney Artificial Intelligence

ISBN 978-951-29-9839-5 (PRINT)
ISBN 978-951-29-9840-1 (PDF)
ISSN 0355-9483 (Print)
ISSN 2343-3213 (Online)
Painosalama, Turku, Finland, 2024

*“We do not know the true value of our moments
until they have undergone the test of memory.”
— Georges Duhamel*

UNIVERSITY OF TURKU

Faculty of Medicine

Institute of Biomedicine

Medical Physics and Engineering

SAMULI ARVOLA: Novel bone SPECT-CT methods — Optimization and validation for imaging bone metastases

Doctoral dissertation, 70 pp.

Doctoral Programme in Clinical Research

August 2024

ABSTRACT

Bone single-photon emission computed tomography (SPECT) combined with X-ray computed tomography (SPECT-CT) is expected to replace planar bone scintigraphy (BS) as the routine method for imaging bone metastases. In preparation for this change, this thesis aimed to optimize and validate novel SPECT-CT methods, including fast whole-body image acquisition using a cadmium-zinc-telluride (CZT) SPECT-CT system, reprojected bone SPECT-CT (RBS), and quantitative SPECT.

Fast image acquisition was optimized by comparing the sensitivity and specificity between SPECT images acquired from the same patients with 50-, 32-, 26-, and 16-min acquisition times. RBS was validated by comparing the sensitivity and specificity between BS and RBS images of the same patients. Quantitative SPECT was validated by comparing standardized uptake values (SUVs) of the same bone metastases between SPECT and positron emission tomography (PET).

The average patient-level sensitivities for the 50-, 32-, 26-, and 16-min images were 88, 92, 100, and 96%, respectively, and the corresponding specificities 78, 84, 84, and 78%, respectively. The average patient-level sensitivities for BS and RBS were 75 and 87%, respectively, and the corresponding specificities 79 and 39%, respectively. SUVs correlated strongly ($R^2 \geq 0.80$) between SPECT and PET.

Whole-body bone SPECT-CT can be performed using a CZT system in less than 20 min without loss of diagnostic performance. Whole-body bone SPECT-CT can be reprojected into planar images with excellent sensitivity but limited specificity for identifying bone metastases. The strong correlation of SUVs between SPECT and PET demonstrates that SPECT SUVs are feasible for uptake measurements in bone metastases.

KEYWORDS: SPECT, SPECT-CT, bone, metastasis

TURUN YLIOPISTO

Lääketieteellinen tiedekunta

Biolääketieteen laitos

Lääketieteellinen fysiikka ja tekniikka

SAMULI ARVOLA: Uudet luuston SPECT-TT-menetelmät — Optimointi ja validointi luustoetäpesäkkeiden kuvantamiseen

Väitöskirja, 70 s.

Turun kliininen tohtoriohjelma

Elokuu 2024

TIIVISTELMÄ

Luuston yksifotoniemissiotomografian (SPECT) yhdistettynä tietokonetomografiaan (SPECT-TT) odotetaan syrjäyttävän tasokuvauksen rutiinimenetelmänä luustoetäpesäkkeiden kuvantamisessa. Tämän muutoksen innoittamana tämä väitöskirja pyrkii optimoimaan ja validoimaan uusia SPECT-TT-menetelmiä, kuten nopea koko kehon kuvaus kadmium-sinkki-telluuri-SPECT-TT-laitteella, SPECT-TT kuvista lasketut tasokuvat ja kvantitatiivinen SPECT.

Nopea kuvaus optimoitiin vertaamalla herkkyyttä ja spesifisyyttä samoista potilaista 50, 32, 26 ja 16 min kuvausajoilla otettujen SPECT-kuvien välillä. Lasketut tasokuvat validoitiin vertaamalla herkkyyttä ja spesifisyyttä samojen potilaiden kuvattujen ja lasketujen tasokuvien välillä. Kvantitatiivinen SPECT validoitiin vertaamalla samojen luustoetäpesäkkeiden standardoituja kertymäärovoja SPECT- ja positroniemissiotomografia (PET) -kuvien välillä.

Keskimääräiset potilastason herkkyydet 50, 32, 26 ja 16 min kuvilla olivat 88, 92, 100 ja 96 % ja spesifisyydet 78, 84, 84 ja 78 %. Keskimääräiset potilastason herkkyydet kuvatuilla ja lasketuilla tasokuvilla olivat 75 ja 87 % ja spesifisyydet 79 ja 39 %. Standardoidut kertymäärvot korreloivat vahvasti ($R^2 \geq 0.80$) SPECT- ja PET-kuvien välillä.

Koko kehon luuston SPECT-TT voidaan kuvata kadmium-sinkki-telluuri-laitteella alle 20 minuutissa ilman diagnostisen suorituskyvyn menetystä. Koko kehon SPECT-TT-kuvasta voidaan laskea tasokuvat, joilla on erinomainen herkkyys mutta rajoitettu spesifisyys luustoetäpesäkkeiden tunnistamisessa. Vahva korrelaatio SPECT- ja PET-kuvien standardoitujen kertymäärovojen välillä osoittaa, että SPECT-kuvien standardoidut kertymäärvot soveltuvat kertymämittauksiin luustoetäpesäkkeissä.

ASIASANAT: SPECT, SPECT-TT, luusto, etäpesäke

Table of Contents

Abbreviations	8
List of Original Publications	9
1 Introduction	10
2 Review of the Literature	12
2.1 ^{99m} Tc-labeled Bisphosphonate	12
2.2 Planar BS	12
2.3 Bone SPECT and SPECT-CT	16
2.3.1 SPECT Reconstruction	16
2.3.2 Hybrid Imaging	21
2.4 Recent Developments in Bone SPECT-CT	24
2.4.1 Semiconductor Detectors	24
2.4.2 List-Mode Acquisition	25
2.4.3 Whole-Body Acquisition	26
2.4.4 Planar Reprojection	27
2.4.5 Quantitation	27
2.4.6 Anatomically Guided Reconstruction	29
2.5 Other Modalities for Imaging Bone Metastases	30
2.5.1 PET-CT	30
2.5.2 CT	31
2.5.3 MRI	32
3 Aims	34
4 Materials & Methods	35
4.1 Patients and Reference Standard Diagnosis	35
4.2 Data Acquisition	36
4.3 Data Processing	37
4.4 Image Analysis	39
4.5 Statistical Analysis	41

5 Results	42
5.1 Optimal Acquisition of Bone SPECT Using a CZT System	42
5.2 Validation of RBS	46
5.3 Validation of Bone SPECT SUVs	48
6 Discussion	52
6.1 Implications for Routine Clinical Practice	52
6.2 Reliability and Validity of the Results	54
6.3 Reflections on Image Acquisition	55
6.4 Reflections on Image Processing	56
6.5 Topics for Further Research	57
7 Conclusions	58
Acknowledgements	59
References	60

Abbreviations

2D	Two-Dimensional
3D	Three-Dimensional
AUC	Area Under the Receiver-Operating Characteristic Curve
BS	Bone Scintigraphy
CI	Confidence Interval
CNR	Contrast-to-Noise Ratio
CT	X-ray Computed Tomography
CZT	Cadmium-Zinc-Telluride
DW-MRI	Magnetic Resonance Imaging with Diffusion-Weighted Imaging
FOV	Field of View
FWHM	Full Width at Half Maximum
IQR	Interquartile Range
LOA	Limits of Agreements
MLEM	Maximum Likelihood Expectation Maximization
MRI	Magnetic Resonance Imaging
OSEM	Ordered Subsets Expectation Maximization
PET	Positron Emission Tomography
PET-CT	Positron Emission Tomography Combined with X-ray Computed Tomography
RBS	Reprojected Bone SPECT-CT
ROI	Region of Interest
SD	Standard Deviation
SPECT	Single-Photon Emission Computed Tomography
SPECT-CT	Single-Photon Emission Computed Tomography Combined with X-ray Computed Tomography
SUV	Standardized Uptake Value
VOI	Volume of Interest

List of Original Publications

This dissertation is based on the following original publications, which are referred to in the text by their Roman numerals:

- I Samuli Arvola, Marko Seppänen, Kirsi L. Timonen, Pentti Rautio, Otto Ettala, Mikael Anttinen, Peter J. Boström, Tommi Noponen. Detection of prostate cancer bone metastases with fast whole-body ^{99m}Tc -HMDP SPECT/CT using a general-purpose CZT system. *EJNMMI Physics*, 2022;9:85.
- II Samuli Arvola, Marko Seppänen, Simona Malaspina, Sorjo Mätzke, Juho Raiko, Kirsi L. Timonen, Otto Ettala, Ivan Jambor, Mikael Anttinen, Anna Kuisma, Eliisa Löyttyniemi, Peter J. Boström, Antti Sohlberg, Tommi Noponen. Comparison of reprojected bone SPECT/CT and planar bone scintigraphy for the detection of bone metastases in breast and prostate cancer. *Nuclear Medicine Communications*, 2022;43:510-517.
- III Samuli Arvola, Ivan Jambor, Anna Kuisma, Jukka Kemppainen, Sami Kajander, Marko Seppänen, Tommi Noponen. Comparison of standardized uptake values between ^{99m}Tc -HDP SPECT/CT and ^{18}F -NaF PET/CT in bone metastases of breast and prostate cancer. *EJNMMI Research*, 2019;9:6.

The original publications have been reproduced with the permission of the copyright holders.

1 Introduction

Metastasis is the ultimate and most lethal manifestation of cancer [1]. Most cancer patients die because of their metastatic disease and not because of primary tumours [2]. Metastasis occurs when a tumour spreads from a primary site to a distinct secondary site within another organ [1]. Bone is the most common site of metastasis for many cancers [3-5].

Prostate and breast cancer cause most bone metastases, up to 70% [6]. This reflects the high incidence and long clinical course of these diseases. Bone metastases are a major cause of morbidity and are characterized by severe pain, impaired mobility, pathological fractures, and spinal cord compression [6]. Imaging has an important role in the detection, diagnosis, prognostication, treatment planning, and follow-up monitoring of bone metastases. The earlier the metastases are discovered, the better they can be treated [7].

Several different techniques can be used for imaging bone metastases. The techniques are categorized into anatomical and functional imaging methods [8]. The anatomical imaging methods include X-ray computed tomography (CT) and magnetic resonance imaging (MRI), and the functional imaging methods include planar bone scintigraphy (BS), single-photon emission computed tomography (SPECT), and positron emission tomography (PET). Functional imaging methods can detect bone metastases several months before they are visualized via anatomical imaging [9]. However, anatomical imaging is highly needed to characterize the nature of functional imaging findings and to distinguish bone metastases from benign lesions [10]. Hybrid imaging methods, SPECT combined with CT (SPECT-CT), PET combined with CT (PET-CT), and MRI with diffusion-weighted imaging (DW-MRI), integrate anatomical and functional imaging. Among the abovementioned imaging methods, planar BS is the only two-dimensional (2D) method, while all the others are three-dimensional (3D).

Planar BS has been the routine method for imaging bone metastases for several decades [11-15]. The method is inexpensive and available in most hospitals. BS has rather high sensitivity for detecting bone metastasis, but the specificity is limited [12, 16, 17]. This issue results in a decrease in diagnostic accuracy and often necessitates additional imaging. A separate CT examination is typically used for radiological confirmation of findings in BS images [18].

Currently, the imaging systems used for planar BS are also capable of SPECT-

CT imaging [10]. SPECT-CT is a more sensitive and specific method than BS [19–21], and SPECT-CT technology is being continuously developed [22]. SPECT-CT is therefore becoming a favorable alternative to BS, possibly to the extent of replacing BS as the routine method for the imaging of bone metastases [23]. However, the use of SPECT-CT has generally been limited to partial-body imaging as an add-on to whole-body planar BS [23]. The widespread adoption of whole-body SPECT-CT has been hindered by the longer examination time and more complex image reporting [10]. Currently, the time required for a whole-body SPECT-CT examination is often more than 40 min, and for BS, it is approximately 15 min [24].

Fortunately, novel SPECT-CT methods have been introduced to overcome these hindrances. Semiconductor detectors enhance the technical performance of imaging systems, possibly allowing for shorter examination times [25]. Moreover, planar reprojection makes 3D SPECT images appear similar to conventional 2D BS images [26], facilitating the transition from routine planar BS to SPECT-CT.

The first two publications included in this thesis focused on increasing the practicality of whole-body bone SPECT-CT. They aimed to optimize and validate SPECT-CT images with shortened examination times and planar images produced by reprojected. The images were evaluated using data acquired from breast and prostate cancer patients at high risk for bone metastases. The patients underwent several different imaging examinations, including planar BS, SPECT-CT, PET-CT, and DW-MRI. The diagnostic accuracy of SPECT-CT images with shortened examination times and reprojected planar images was validated against a reference diagnosis, which is mostly based on PET-CT and DW-MRI. These are considered the most accurate methods currently available for imaging bone metastases [19, 20, 27]. However, PET-CT is more expensive and less available than SPECT-CT [28], and DW-MRI requires a long examination time [29–31].

Conventional image interpretation of bone SPECT-CT is purely visual, which means that no quantitation is performed [32, 33]. On the other hand, PET-CT routinely provides numeric values representing the rate of metabolism in bone metastases [34–38]. Therefore, the third publication included in this thesis aimed to validate quantitative SPECT as a novel method by comparing quantitative measurements of bone metastases between SPECT and PET images.

This thesis begins with a literature review on the basic principles of BS, SPECT, PET, CT, and MRI. Additionally, theoretical aspects and previous research on novel SPECT-CT methods are revised. The remainder of this thesis is a summary and discussion on the experimental work aiming to optimize and validate novel methods, which include semiconductor detectors, planar reprojected, and quantitative SPECT.

2 Review of the Literature

2.1 ^{99m}Tc -labeled Bisphosphonate

Both planar BS and bone SPECT begin with intravenous injection of the radiopharmaceutical ^{99m}Tc -labeled bisphosphonate [24]. ^{99m}Tc is a radionuclide with a physical half-life of six hours [39]. ^{99m}Tc decays to ^{99}Tc by isomeric transition and emits one 140-keV gamma ray per decay [40]. The activity of the radiopharmaceutical agent is usually between 500 and 1100 MBq at the time of injection [41].

The radiolabeled bisphosphonates injected into the blood circulation adsorb to the surface of hydroxyapatite crystals in proportion to local bone vascularization and osteoblastic activity. The maximum bone accumulation is reached 1 h after the injection and remains practically constant for up to 72 h [24]. However, imaging is delayed for at least another hour to allow clearance of unbound radiopharmaceutical into the urine. Four hours after injection, approximately 60% of the injected radiopharmaceutical is fixed in the skeleton, 34% is excreted in the urine, and only 6% remains in the circulation [24].

2.2 Planar BS

Imaging is performed 2–4 h after the injection using a SPECT or SPECT-CT system [41]. Both systems consist of a patient bed and typically two gamma camera detector heads [42]. A SPECT-CT system additionally includes an integrated CT scanner, which is not used in a planar BS examination. The patient lies on the bed, which is moved between the detector heads, and the gamma rays emitted from the patient are measured.

A detector head consists of a lead collimator, the detector itself, and electronics [43]. A collimator ensures that only perpendicularly arriving gamma rays reach the detector by absorbing oblique gamma rays [44]. Most of the gamma rays are either emitted away from the detector head or absorbed by the collimator. Only 0.01% of the emitted gamma rays reach the detector [45]. The collimator consists of 1–2 mm wide and 20–40 mm long holes separated by 0.1–0.2 mm thick lead septa [46]. These are the parameters of a typical low-energy high-resolution collimator used in BS and bone SPECT. Collimators for other applications include, for example, high-energy collimators with thicker septa and longer holes and high-sensitivity collimators with

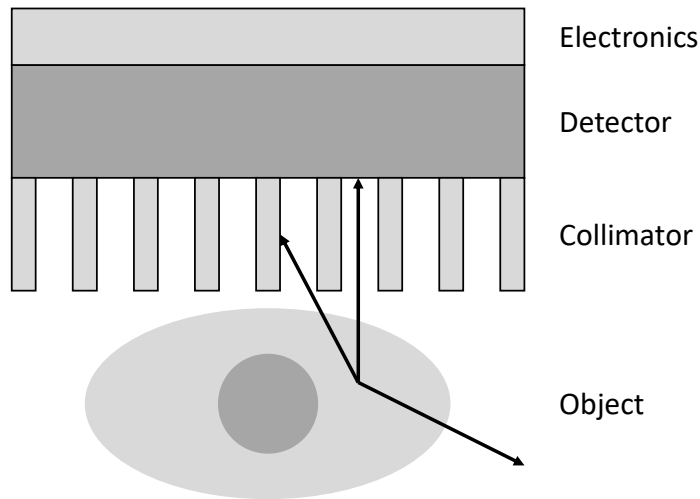


Figure 1. Structure of the SPECT system detector head. The arrows denote gamma rays emitted from the object.

shorter and more numerous holes.

The detector converts gamma rays into an electric signal. The details of the detector structure are discussed in section 2.4.1. The electronics contain the circuits required for determining the gamma-ray energy and position on the surface of detector. The image is then formed as the 2D distribution of the gamma rays absorbed by the detector. A schematic of the detector head is shown in Figure 1.

Planar BS is usually performed as a whole-body examination and requires covering an area up to 50 cm \times 200 cm. However, the typical field-of-view (FOV) of a gamma camera is only 50 cm \times 40 cm [46]. Covering the entire skeleton therefore requires the acquisition of multiple FOVs. These separate FOVs are acquired by moving the bed. The movement can be either continuous or stepwise.

In a planar BS examination, two images are acquired using two detector heads. One is acquired from the anterior side of the patient, and the other from the posterior side (Figure 2) [24]. These images are essentially 2D projections of the 3D activity distribution within the patient. However, projections are affected by various physical phenomena, including gamma-ray attenuation and scattering in tissue [47]. Furthermore, the spatial resolution of the collimator decreases as the distance to the emission source increases [48]. Image acquisition requires consideration of several technical factors, including acquisition time, matrix size, and energy window.

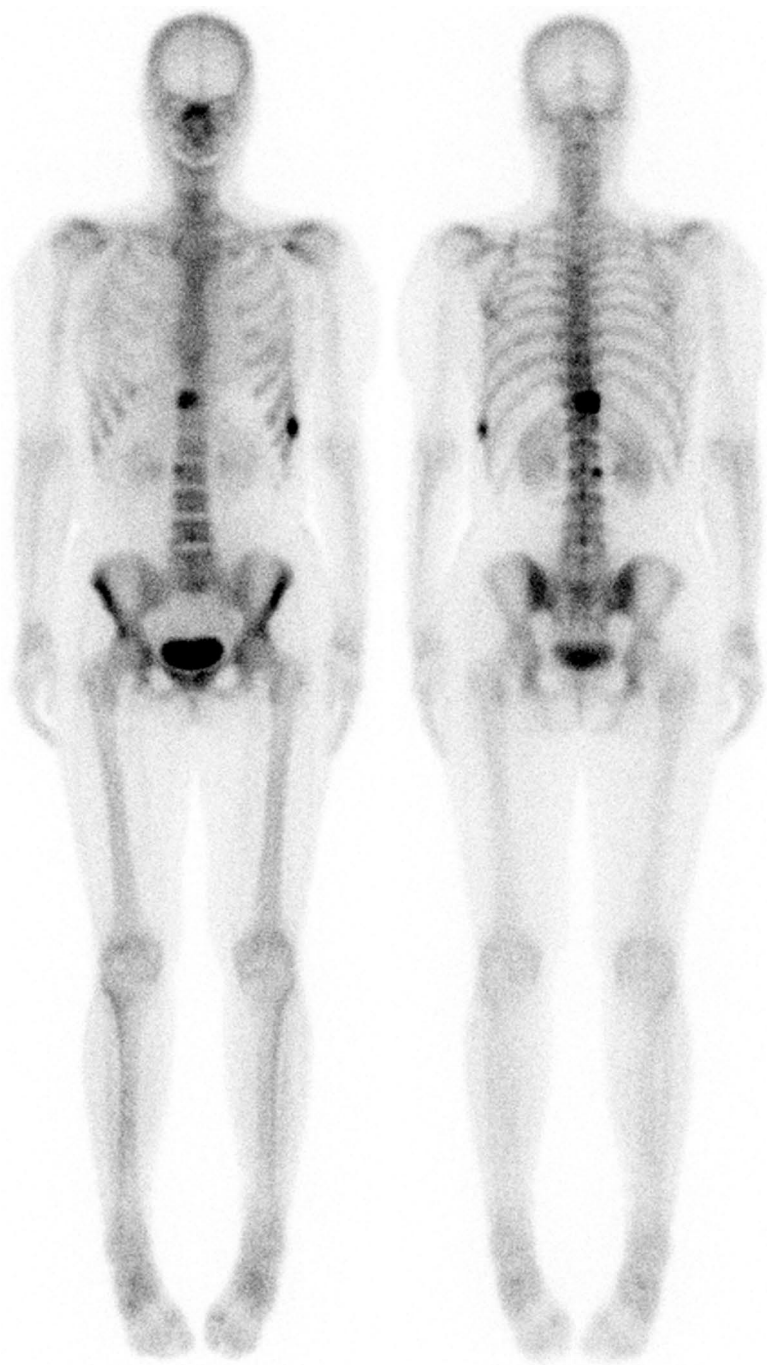


Figure 2. Anterior (left) and posterior (right) planar BS images of a 50-year-old breast cancer patient with visible bone metastases in spine and rib.

Acquisition Time

The required acquisition time depends on the injected activity, patient body weight, and desired image noise level. A higher injected activity increases the rate at which gamma rays are emitted and detected. The required acquisition time is therefore inversely proportional to the injected activity [49]. A greater patient weight increases gamma-ray attenuation in tissue, and fewer gamma rays reach the detector. A longer acquisition time or higher injected activity is therefore required for larger patients.

Image noise is inversely proportional to the square root of the number of detected gamma rays [50]. Instead of adjusting the acquisition time or injected activity separately for each patient, they can be set constant such that the image noise level is acceptable for larger patients and better for smaller patients. The speed of the continuous movement or time per view in stepwise acquisition defines the total acquisition time of a BS examination. The typical acquisition time for a 70 kg patient with 700 MBq injected activity is 15 min.

Matrix Size

The image matrix size is 256×1024 or 512×2048 [24]. A larger matrix has a smaller pixel size, which allows for improved spatial resolution but also increases noise [51]. The pixel size is typically 2–5 mm, which is close to the intrinsic spatial resolution of the detector [48]. A larger matrix size also requires more computing power, especially in SPECT [52].

Energy Window

The energy window specifies the accepted energy range of the detected gamma rays. Gamma rays scatter and change direction within the body, leading to the loss of energy during the process. The most relevant scattering phenomenon is Compton scattering, in which the gamma-ray energy decreases such that:

$$E' = \frac{E}{1 + \frac{E}{511 \text{ keV}}(1 - \cos \theta)}, \quad (1)$$

where E' is the energy of the scattered gamma ray, E is the energy before scattering, and θ is the scattering angle [53].

Energy window setting provides a means to discriminate against gamma rays that have been scattered within the body and therefore lost their positional information. By choosing a relatively narrow energy window centred at 140 keV, only gamma rays that undergo no scattering or small-angle scattering will be accepted. The energy resolution of a typical scintillator-based SPECT detector is 10%, determined as the full width at half maximum (FWHM) of the measured photopeak. The energy window is usually 15 or 20% wide [54].

2.3 Bone SPECT and SPECT-CT

The limited depth information of BS hinders accurate anatomical localization of radiopharmaceutical uptake. This limitation can be overcome using bone SPECT, which is essentially BS extended into three dimensions [18]. SPECT is a tomographic imaging method, in which a 3D object is viewed as a stack of 2D slices [55, 56].

The radiopharmaceutical principle is the same for BS and bone SPECT [57]. In fact, bone SPECT is typically performed immediately after planar BS as a complementary examination. The technical considerations listed for BS also apply to bone SPECT. However, a longer acquisition time may be required in bone SPECT than in BS, and the matrix size is reduced to 128×128 [24].

The most obvious difference between BS and SPECT acquisitions is the rotation of the detector heads during SPECT. The detector heads rotate around the patient, acquiring projections over several angles and often covering a full 360-degree rotation [15]. An example of a typical SPECT acquisition is 120 projections with a 3-degree interval, with each projection being acquired for 10–20 s. The total acquisition time is 13–24 min per FOV including idle time caused by the detector movements.

While multiple FOVs and whole-body coverage are routine in BS, a single FOV is often used in SPECT, covering only 40 cm of the body length [23]. The anatomical coverage of this FOV is determined according to the findings in the previously acquired BS images. Multiple FOVs can be applied in SPECT, but this greatly increases the examination time [58].

2.3.1 SPECT Reconstruction

Image processing, especially reconstruction, is a fundamental aspect of SPECT and other tomographic imaging methods. In BS, the acquired anterior and posterior projections can be viewed as such without further processing. In SPECT, however, the acquired projections are converted into cross-sectional slices using a reconstruction algorithm [59].

The projection data corresponding to a slice are commonly represented as a sinogram [59]. In the sinogram, the horizontal axis represents the position on the detector, and the vertical axis corresponds to the angular position of the detector. The corresponding number of detected gamma rays is assigned to each point of the sinogram. In addition to images, sinogram and slice can be considered vectors. In this case, the relationship between the sinogram and slice can be concisely represented as the matrix product:

$$\mathbf{g} = \mathbf{A}\mathbf{f}, \quad (2)$$

where vector \mathbf{g} is the sinogram with elements g_i , matrix \mathbf{A} is the projection operator with elements a_{ij} , and vector \mathbf{f} is the slice with elements f_j . Reconstruction

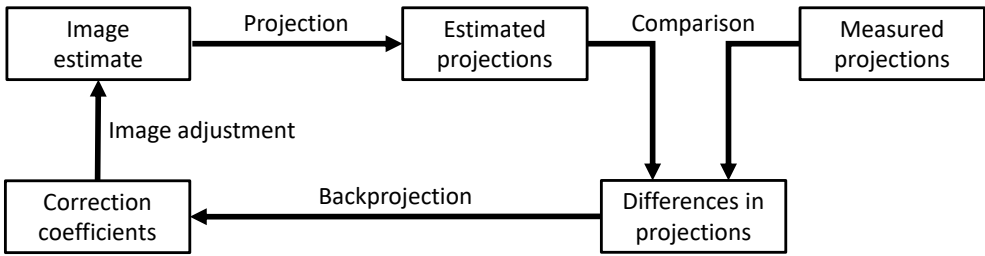


Figure 3. The basic principle of iterative reconstruction. The corrections for attenuation, scatter, and collimator response are performed during the projection and backprojection steps.

algorithms aim to solve this equation for f .

Currently, bone SPECT data are reconstructed using iterative algorithms [24], which find the solution to equation (2) by successive estimates [59]. The algorithms differ in the way the measured and estimated projections are compared and the kind of correction applied to the current estimate. The process is initiated by an arbitrary first image estimate, which can be a uniform image. The image estimate is then projected to obtain the estimated projections, which are compared with the measured projections. The difference between the estimated and measured projections is back-projected, and the image estimate is adjusted according to this difference [60]. The adjusted image estimate becomes the new initial estimate for the second iteration and the same process is repeated for multiple iterations until a final solution or a predetermined number of iterations is reached [61]. The cycle of iterative reconstruction is presented in Figure 3.

The most widely used reconstruction algorithm in SPECT is the ordered subsets expectation maximization (OSEM) algorithm [62], which is an accelerated form of the maximum likelihood expectation maximization (MLEM) algorithm [63, 64]. A particular advantage of these algorithms is the underlying assumption that the measured data are subject to Poisson noise. This is true for the acquired SPECT data, as they are affected by uncertainty resulting from the Poisson statistical variations of radioactive decay [65]. Consequently, sinogram \mathbf{g} corresponds to a specific measurement, and if statistical phenomena are not considered, slice f is the specific solution corresponding to that specific sinogram \mathbf{g} .

The MLEM algorithm aims to find a general solution as the best estimate for f , that is, the slice that can produce sinogram \mathbf{g} with the highest likelihood. The MLEM algorithm follows the cycle described in Figure 3. The algorithm is defined by the following equation:

$$f_j^{\text{new}} = \frac{f_j^{\text{old}}}{\sum_i a_{ij}} \sum_i \frac{g_i}{\sum_j a_{ij} f_j^{\text{old}}} a_{ij}, \quad (3)$$

where f_j^{new} and f_j^{old} are the current and previous image estimates, respectively [60].

A detailed derivation of the equation beginning from the Poisson distribution is presented by Lange and Carson in [64]. Central to the algorithm is the projection operator a_{ij} , which models the underlying physics of the detection process by describing the probabilities that gamma rays emitted from specific object voxels will be detected at specific detector pixels. The system model can account for the collimator geometry and incorporate physical factors such as the attenuation of gamma rays [66].

Attenuation Correction

Attenuation distorts the acquired image by decreasing the number of detected gamma rays [67]. The magnitude of attenuation depends on the length and density of the tissue through which the gamma rays travelled. The attenuation can be expressed by the following equation:

$$I = I_0 \cdot \exp \left(- \sum_i \mu_i x_i \right), \quad (4)$$

where the index i represents all the different tissue regions along the gamma-ray trajectory, μ_i are the attenuation coefficients for the regions, and x_i are the corresponding thicknesses of the regions. The sum represents the total attenuation through all tissue regions [67].

Attenuation correction is performed by including gamma-ray attenuation in the system model during reconstruction. This requires a complete distribution of the linear attenuation coefficients within the body, i.e., an attenuation map. A CT image acquired during SPECT-CT is essentially a distribution of attenuation coefficients in the patient [68]. However, attenuation coefficients are energy-dependent, and images present them as CT numbers on the Hounsfield scale. The CT number relates the tissue attenuation coefficients to the attenuation coefficients of water and air such that:

$$\text{CT number} = \frac{\mu_{\text{tissue}} - \mu_{\text{water}}}{\mu_{\text{water}} - \mu_{\text{air}}} \cdot 1000 \text{ HU}, \quad (5)$$

where μ_{tissue} , μ_{water} , and μ_{air} are the attenuation coefficients for tissue, water, and air, respectively, at the specific energy of X-rays, and HU is the Hounsfield unit.

The energy of X-rays in CT ranges between 80–130 keV, and the energy of gamma rays in bone SPECT is 140 keV. Before the CT image is used as the attenuation map, it is converted to linear attenuation coefficients at 140 keV. This is achieved by acquiring a CT image of a phantom containing materials whose attenuation coefficients at 140 keV are known. The HU values for these materials are then defined, and the relationship between attenuation coefficients at 140 keV and HU values is modeled bilinearly, resulting in separate calibration equations for bone and soft tissue [69, 70].

Scatter Correction

The main phenomenon that leads to scatter in SPECT images is Compton scattering. The effects of coherent scattering are negligible and are usually ignored [71]. In Compton scattering, a gamma ray interacts with tissue, loses energy, and changes direction. A gamma ray can scatter multiple times. The consequence of Compton scattering is that the gamma ray may be detected at the wrong position on the detector or not detected at all [67]. Scattering reduces image contrast and quantitative accuracy [71].

Scatter compensation is probably the most challenging of all the compensations. The scatter contribution is dependent on several factors: activity distribution, attenuation map, detector energy resolution, and energy window [72]. The scatter-spread-function is therefore difficult to parametrize.

Two different approaches are used for scatter correction in bone SPECT: the energy-window-based approach and the reconstruction-based approach. In the energy-window-based approach, the scattered gamma rays are measured using additional energy windows placed below, and possibly also above, the primary photo peak window [73]. The scatter window data are then either subtracted from the primary window or used in the projection step of the iterative reconstruction as an estimate of scatter [74].

The reconstruction-based approach utilizes an attenuation map and Monte Carlo simulation to model scattering [75–77]. The advantages of this approach include better image contrast and lower noise levels than those of energy-window-based approach [77]. The challenge of the reconstruction-based approach is the increased computational requirement. The scatter estimation is incorporated directly into the projection operator matrix, which becomes considerably larger and slows down the computation [78].

This can be overcome with the dual-matrix approach, in which scatter is incorporated only in the forward projection step [79]. This method requires that the scatter response function is computed at each point in the reconstructed volume for all projection views and iterations. To further accelerate the computation, the correction factors can be calculated only once or a few times, given that the calculated scatter component is practically constant after the first few iterations [80]. The equation of the MLEM algorithm can then be written as:

$$f_j^{\text{new}} = \frac{f_j^{\text{old}}}{\sum_i a_{ij}} \sum_i \frac{g_i}{\sum_j a_{ij} f_j^{\text{old}} + s} a_{ij}, \quad (6)$$

where s is the scatter estimated on all projections [74].

Collimator Response Correction

The collimator response is the dominant factor affecting the overall spatial resolution of SPECT [81]. At the face of the collimator, the resolution is close to that of the detector, between 2.5 and 4 mm. However, the resolution degrades as the distance between the collimator and gamma-ray source increases, ranging from 7 to 15 mm with clinically relevant distances [43].

Collimator response correction reduces this degradation. A common method for correction is to model the response during iterative reconstruction, for example, by convolving the reconstructed pixel with the collimator response function before projection [82]. The response function is usually assumed to be a 2D Gaussian function, whose FWHM depends on the detector resolution, collimator hole length, collimator hole diameter, and distance to the point of gamma-ray emission [66, 82, 83].

Convergence and Noise

During the first 20 to 40 iterations, the MLEM algorithm converges towards an acceptable reconstruction. During the later iterations, the likelihood still increases but the reconstructions also get noisier. This is caused mainly by the Poisson statistical variation in the measured projections. A reconstruction corresponding to noisy measurement data will be even noisier because the projection operator acts as a smoothing operator [61].

Different techniques for solving this problem have been investigated. One possible approach is to limit the possible reconstructions to the ones which are smooth enough [84]. A second solution is to perform many iterations and postfilter the reconstruction [85]. A third approach is to stop the reconstruction early while the noise level is still acceptable [61]. For clinical use, mostly the postfiltering method is used, and Gaussian or Butterworth filter is typically applied [85–87]. The Gaussian filter is defined by the FWHM, and the Butterworth filter by the order and cutoff frequency.

Convergence of the MLEM algorithm is frequency dependent. Low spatial frequencies converge faster than higher frequencies. This is due to the low-pass effect of the projection operation. It follows that reducing the number of iterations has an effect similar to reducing the cutoff frequency of a low-pass filter. The noise in the higher MLEM iterations is high frequency noise. As a result, a modest amount of smoothing adequately suppresses the noise at the cost of a mild loss of resolution [61].

The spatial resolution improves with increased iterations, and if the reconstruction includes collimator response correction, the resolution can be eventually better in the reconstructed image than in the acquired projections. Increasing the number of iterations can increase the noise significantly. However, the postfiltered image has a nearly position-independent and predictable spatial resolution. Thus, if SPECT

images are acquired for quantification, it is reasonable to use an adequate number of iterations and postprocessing filtering, rather than a reduced number of iterations, for noise suppression [61].

The MLEM algorithm has proven to be effective, but also too slow for the daily routine. Depending on the settings of the algorithm and the desired convergence, 10 to 100 iterations are usually required [61]. Even with modern computer central processing units, this requires a calculation time of approximately 3 to 30 minutes.

OSEM Algorithm

The OSEM algorithm was proposed by Hudson and Larkin to accelerate the reconstruction [62]. With this method, the set of projections is divided into subsets, each of which contains projections distributed equally around the patient. The MLEM algorithm is subsequently applied to each subset as a subiteration. The image is updated sequentially such that the result of a previous subset is used as an initial estimate for reconstruction with the next subset. The first full iteration is complete when all the subsets have been processed.

The OSEM algorithm converges to an image that is nearly identical to the image reconstructed with the MLEM algorithm, but it requires fewer iterations and is thus faster [62]. The acceleration achieved is proportional to the number of subsets used. For example, the use of 15 subsets would accelerate convergence by a factor of 15 compared with the MLEM algorithm. However, convergence requires that each subset contains at least four projections, i.e., a maximum of 30 subsets for data acquired using 120 projections [88]. Convergence of OSEM algorithm also requires consistent data and subset balance, which means that all voxels contribute equally to all subsets [62]. In practice, these conditions are never met, and OSEM algorithm can be shown to converge to a limit cycle rather than a unique solution, with the result that the OSEM reconstruction is noisier than the corresponding MLEM reconstruction. However, the difference between the two is not clinically relevant [61].

The numbers of iterations and subsets applied in the OSEM algorithm are usually chosen according to manufacturer recommendation or local preference. A recent study aiming to optimize image quality in bone SPECT-CT suggested that 12 iterations, 8 subsets, and a postprocessing Gaussian filter with 8-mm FWHM provide an optimal balance between noise and spatial resolution [87].

2.3.2 Hybrid Imaging

BS and bone SPECT are functional imaging modalities, which means that they focus on imaging tissue metabolism. However, their anatomical imaging capabilities are limited, especially for small structures [89]. For CT, this is reversed. CT is an anatomical imaging modality with excellent spatial resolution, but it provides little

information on tissue metabolism [90]. Most modern SPECT systems are in fact SPECT-CT systems with integrated CT scanners [91]. Bone SPECT examination can therefore be complemented by a CT examination.

On SPECT-CT, CT can be acquired immediately before or after SPECT [24]. The patient lies on the bed and ideally does not move between the two acquisitions. For CT, the bed is moved inside the CT scanner of the SPECT-CT system. There, X-rays with energies ranging from 80 to 130 keV are emitted and detected on the opposing sides of the patient by the X-ray tube and detector, respectively [24]. The X-ray tube and detector rotate around the patient, and projections are acquired, similar to SPECT.

However, while the tissue attenuation of gamma rays is an undesired phenomenon in SPECT, the attenuation of X-rays forms the basis for CT projections. Specifically, the CT projection data correspond to the transmission of X-rays through an object [92]. In addition, CT projections are acquired at a much higher rate than SPECT projections and are more numerous. A single 360-degree rotation in CT takes less than a second [93], while in SPECT, it takes several minutes. The number of acquired projection angles during a single rotation ranges from 60 to 120 on SPECT and from 1000 to 2500 on CT [94, 95]. The bed movement can be continuous during CT acquisition, causing the X-ray tube and detector to perform helical trajectories relative to the bed [96]. The CT image is acquired from the same anatomical area as the SPECT image. The total acquisition time for CT is only a few seconds if the preparation time is not considered [97].

The CT projection data are reconstructed using conventional filtered back projection or iterative algorithm with the same basic principles as those presented for SPECT in Figure 3 [98, 99]. The reconstructed image represents a distribution of the linear attenuation coefficients inside the body [68]. The attenuation coefficients and high spatial resolution provided by CT images can be used to enhance SPECT reconstruction as further discussed in sections 2.4.5 and 2.4.6.

For image interpretation, SPECT and CT images are displayed simultaneously, with one overlaid on top of the other. Fused 3D SPECT-CT images are usually displayed as 2D slices from orthogonal planes and SPECT as maximum intensity projection (Figure 4). Maximum intensity projection is a visualization method for 3D data that projects in the visualization plane the voxels with maximum intensity that fall in the way of parallel rays traced from the viewpoint to the plane of projection. The resulting 2D projection provides limited visualization of depth. To improve the 3D visualization, maximum intensity projections can be rendered from several angles and viewed as a rotating animation.

A major advantage of hybrid imaging is the potential to distinguish benign and metastatic radiopharmaceutical uptake [18]. Increased focal uptake on SPECT may correspond to several different conditions, each of which has a characteristic appearance on CT.

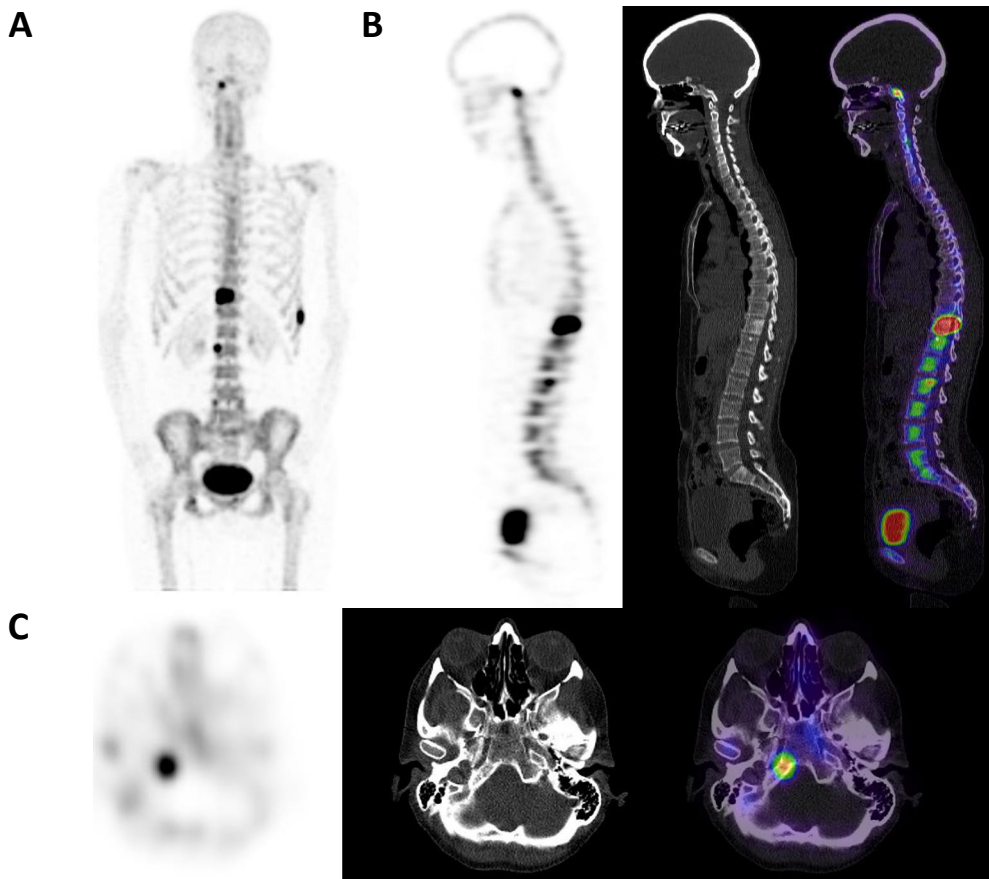


Figure 4. Maximum intensity projection (A), sagittal SPECT, CT, and SPECT-CT images (B), and axial SPECT, CT, and SPECT-CT images (C) of a 50-year-old breast cancer patient with visible bone metastases in spine, rib, and pelvis.

2.4 Recent Developments in Bone SPECT-CT

2.4.1 Semiconductor Detectors

Recent developments in SPECT instrumentation have been driven mainly by the advent of semiconductor detectors. They directly convert gamma rays into electrical signals utilizing the unique properties of semiconductors. Cadmium-zinc-telluride (CZT) is one of the most established semiconductor detector materials [100].

In conventional scintillation detectors, Tl-activated NaI crystal absorbs gamma rays and converts them into visible light. The photomultiplier tube converts light into an electrical signal and amplifies it. Multiple photomultiplier tubes form an array behind the crystal. The amount of electrical signal produced in a photomultiplier tube is proportional to the amount of light it receives, which in turn depends on the distance to the position where the gamma ray interacts with the crystal. The spatial location of the gamma-ray detection is determined by combining the electrical signal from each photomultiplier tube in a logic circuit that weights the signals appropriately [101-103].

In CZT semiconductor detectors, gamma rays deposit energy into pixelated semiconductor crystal, generating charge carriers. An electric field is applied to sweep the charge carriers to the anode and cathode, and a current pulse is induced. The spatial location of the gamma ray is determined directly as the location of the interacting detector pixel. The physical properties of the CZT detector allow for several improvements over those of conventional scintillation detectors, including improved energy resolution, spatial resolution, stopping power, and size.

The energy resolutions of the CZT and NaI detectors in modern SPECT-CT systems are approximately 6 and 10%, respectively [104]. The energy resolution of both detectors is partly determined by the number of secondary particles produced, i.e., the number of photons in NaI and the number of charge carriers in CZT [102]. The number of charge carriers produced in CZT is an order of magnitude greater than the number of photons produced in NaI. The energy resolution is ultimately limited by Poisson statistical uncertainties [105].

Two advantages are obtained with the improved energy resolution of CZT. First, when the photopeak narrows, unscattered gamma rays are detected more probably within the chosen energy window. Second, scattered gamma rays are rejected more probably because their energy spectrum narrows too. Thus, the ratio of unscattered to scattered gamma rays is increased, and image quality is improved.

The intrinsic spatial resolutions of the CZT and NaI detectors in modern SPECT-CT systems are approximately 2.5 and 4 mm, respectively [106]. The difference in resolution is caused partly by the difference in length travelled by the secondary particles. In CZT, a compact charge cloud is detected by a segmented anode that is only millimetres away [107]. On the other hand, the photons in a NaI crystal diffuse over a considerable distance before being detected, and the photomultiplier tubes

used for locating photons may be more than a centimetre away from the point of gamma-ray interaction [108].

The linear attenuation coefficient of CZT is greater than that of NaI, potentially leading to increased stopping power and gamma-ray sensitivity [43]. However, due to cost and technical considerations, clinical CZT detectors are thinner than scintillators and therefore have comparable sensitivity in practice [109].

Nonetheless, the overall sensitivity and spatial resolution of a SPECT detector head tend to be dominated by the collimator used. Due to the higher intrinsic spatial resolution of a CZT detector, the collimator of a CZT system can be designed to have higher sensitivity at the cost of spatial resolution. In this way, the CZT system can have improved sensitivity compared to the conventional system when their spatial resolutions are matched [110]. The improved sensitivity allows for short acquisition time or low injected activity.

Finally, and perhaps most importantly, the small size of the CZT detector enables nonstandard detector configurations and system architectures to attain further improved performance. In fact, the first clinical CZT SPECT systems were based on novel system architectures dedicated to breast and cardiac imaging [106, 111]. General-purpose CZT SPECT systems, with novel and conventional system architectures, were introduced only a few years later [48, 112].

Previous research on CZT SPECT has focused mainly on cardiac imaging systems, leading to recently published systematic reviews and meta-analyses on their diagnostic performance [113-115]. Research on bone imaging with CZT systems is scarce, consisting of technical system performance measurements [104, 116] and visual impressions from reduced acquisition time images [25, 117, 118].

2.4.2 List-Mode Acquisition

The projection data in SPECT can be acquired and stored using frame mode or list mode. Frame mode is more commonly used because it is more straightforward and requires less computer memory. List mode, on the other hand, is better suited for optimization and research purposes as new data sets corresponding to different acquisition parameters can be generated from a single acquisition [119].

In frame mode, a matrix corresponding to locations on the detector is created before acquisition starts. During the acquisition, a matrix element is incremented each time a gamma ray is detected on the corresponding location on the detector. This continues until a preselected time interval or number of detected gamma rays is reached. The computer memory required for a frame-mode acquisition is determined by the matrix size and the number of acquired frames, which is the number of projection angles multiplied by the number of axial FOVs [119].

In list mode, the detection time, location, and energy of each gamma ray are stored in a list. The list data can be then resampled into a matrix, in the manner

described above, to produce projection data with chosen acquisition parameters. In some modern software, the acquisition parameters used in the resampling can be chosen freely within the limits of original acquisition. A disadvantage of list-mode acquisition is the required computer memory, which is an order of magnitude greater than that of frame-mode acquisition [119].

2.4.3 Whole-Body Acquisition

Bone SPECT-CT is typically performed as a partial-body examination complementing routinely performed whole-body planar BS. However, whole-body SPECT-CT is expected to become a new routine method in the near future [10, 23, 58, 120, 121]. Whole-body SPECT improves sensitivity compared to planar BS, and SPECT-CT improves specificity and diagnostic confidence compared to SPECT [19, 20, 27, 122–127].

In a recent study including 53 patients [19], the patient-level sensitivities of whole-body BS, SPECT, and SPECT-CT were 79, 89, and 89%, respectively, when equivocal findings were omitted, and 85, 95, and 95%, respectively, when equivocal findings were considered metastases. The corresponding specificities were 91, 80, and 94%, respectively, when equivocal findings were omitted, and 59, 56, and 88%, respectively, when equivocal findings were considered metastases. The values of BS and SPECT-CT are similar to a recent meta-analysis of 11 studies with a total of 1611 patients [121]. SPECT without CT was not included in the meta-analysis.

The improved sensitivity is caused by the 3D nature and higher contrast of SPECT images [52, 128], and the improved specificity is caused by anatomical characterization of findings in CT images [18]. The improved sensitivity and specificity allow for more accurate staging of the extent of bone metastases, selection of treatment, and assessment of treatment response [129, 130].

Despite these benefits, the use of whole-body bone SPECT-CT has been limited, partially due to the lack of fast acquisition protocols. The acquisition time of whole-body SPECT-CT is approximately 45 minutes if the typical acquisition parameters of partial-body SPECT-CT are applied. Fortunately, novel CZT SPECT systems allow for faster acquisition, which could facilitate the adoption of whole-body SPECT-CT [22]. Another drawback of whole-body SPECT-CT is the increased radiation exposure caused by extended CT coverage. The radiopharmaceutical injection in BS and bone SPECT causes a radiation exposure of approximately 4 mSv, and CT causes an additional radiation exposure of approximately 3 mSv [24].

Technically, whole-body bone SPECT-CT does not normally cover the entire skeleton. Instead, three or two FOVs are typically acquired, covering the area from the skull vertex to the mid-thigh or from the cervical region to the proximal femur, respectively [121]. The distal lower extremities can be usually omitted from imaging because the incidence of solitary metastasis below the femur is low [131].

2.4.4 Planar Reprojection

SPECT-CT provides more complex information than planar BS. Therefore, the transition from planar imaging to SPECT-CT may be met with reluctance as some physicians hesitate to abandon the familiar methodology of BS. Both BS and whole-body SPECT-CT could be acquired in a row during this transition period, but the total examination time would greatly increase. Fortunately, planar images can be algorithmically generated from reconstructed SPECT images [26]. The algorithm essentially projects the SPECT image to anterior and posterior detector positions and models attenuation.

Furthermore, modern SPECT-CT systems with ring-shaped detector configurations acquire data only as SPECT and are incapable of planar acquisition. With these systems, reprojection is the only way to obtain planar images [132, 133]. Planar reprojection has been previously validated only for lung [134-137] and gated blood-pool imaging [138, 139].

2.4.5 Quantitation

The base unit in SPECT images is the count, i.e., the number of gamma rays detected from a volume element, a voxel [140-142]. The number of counts in a voxel is proportional to the radiopharmaceutical activity concentration in that location. However, the proportionality can be ambiguous because gamma-ray attenuation, scatter, and collimator response cause distortions in the number of counts. For this reason, SPECT has been traditionally regarded as non-quantitative, and image interpretation has been based on visual evaluation of relative intensity differences [32, 143].

When hybrid SPECT-CT systems became widely available, quantitative SPECT gained interest [32]. CT images provide reliable patient-specific attenuation correction, which is a key requirement for quantitative SPECT. Another development promoting quantitative SPECT was the increase in computing power, which allowed the inclusion of various corrections in iterative reconstruction [143].

Sensitivity Calibration

The purpose of sensitivity calibration is to determine the ratio between the gamma-ray detection rate and activity in the FOV. The calibration can be performed using planar acquisition from a point or petri-dish source or SPECT acquisition from a large uniform cylinder source [144]. The source activity is measured using a dose calibrator, which is the device used to measure the radiopharmaceutical activity administered to a patient. SPECT images are quantitative when the acquired counts have been reconstructed, corrected to be physically accurate, and converted to units of radiopharmaceutical activity concentration in Bq/ml [32, 140-143].

Quantitative Bone SPECT

Radiopharmaceutical uptake in bone represents the rate of bone metabolism, which is increased in various pathological conditions, including bone metastases [145]. Conventionally, the interpretation of bone SPECT has been based on the visual assessment of relative differences in radiopharmaceutical uptake. However, visual assessment is subjective and prone to interobserver variability. On the other hand, quantitative measurements of radiopharmaceutical uptake could provide a more objective interpretation and reduce uncertainty [146].

The radiopharmaceutical activity concentration is affected by the administered activity and distribution volume. Voxel values are therefore normalized with respect to administered activity and distribution volume, which is often substituted by patient weight [147, 148]. This normalization yields standardized uptake values (SUVs). Technically, the SUV is a semiquantitative measure, because it is based on the ratio of activity concentration to total injected activity, and the possible bias in measured activity will cancel out [149, 150].

The earliest attempts at bone SPECT quantitation were demonstrated a few decades ago [151–154]. However, the reconstructions were rather rudimentary and did not include any physical corrections. Nonetheless, accurate measurements of activity concentration in the skull were demonstrated after sensitivity calibration [151]. Additionally, quantitative measurements correlated with the severity of endocrine abnormalities [152] and could predict bone loss in patients with osteoporosis [153] and chronic renal disease [154].

During the last decade, research on quantitative bone SPECT has been increasing due to commercially available quantitation software. The latest research has focused on SUV measurements of normal vertebrae [33, 147], the repeatability of SUVs [155], the differentiation of bone metastases from benign findings [156–163], longitudinal evaluation of treatment response [146, 164–167], evaluation of bone metastatic burden [168], detection of loose prostheses [169], and severity assessment in osteoarthritis [170], osteoporosis [171], and growth disorder [172]. Furthermore, several reviews on quantitative SPECT have been published [32, 148, 173, 174].

While SPECT quantitation is novel, PET quantitation is common, and SUVs are routinely used in PET image interpretation [34]. Therefore, bone PET with ^{18}F -NaF is a potential reference standard for the validation of quantitative bone SPECT. ^{18}F -NaF PET has been validated against biopsy [35, 36] and proven to be repeatable in patients with bone metastases [37, 38].

2.4.6 Anatomically Guided Reconstruction

The CT image acquired via SPECT-CT is primarily used for anatomical characterization and attenuation correction. However, the anatomical information from CT images can also be utilized to guide SPECT reconstruction to improve spatial resolution. Two approaches for anatomically guided reconstruction have been recently introduced. The first is a Bayesian method, which includes differences between adjacent CT voxels in the reconstruction [175-178]. The other is a zonal mapping method, which divides SPECT voxels into different tissue zones according to the corresponding CT voxel values [179-181]. The different zones are then projected separately and backprojected together during iterative reconstruction [181].

Anatomically guided SPECT reconstruction allows for more accurate delineation of radiopharmaceutical uptake in bone [182], which has been shown to improve quantitation accuracy [176, 180], metastasis detection [178], and diagnostic confidence [158, 183]. The method has also been used for acquisition time reduction [184]. A drawback of anatomically guided reconstruction is the increased computational complexity. This is primarily caused by the requirement of a 256×256 matrix [176, 185]. Fortunately, reconstruction can be greatly accelerated by running the algorithm on a graphics processing unit instead of the central processing unit of the computer [186]. A comparison of images reconstructed using a conventional OSEM algorithm and an anatomically guided algorithm is shown in Figure 5.

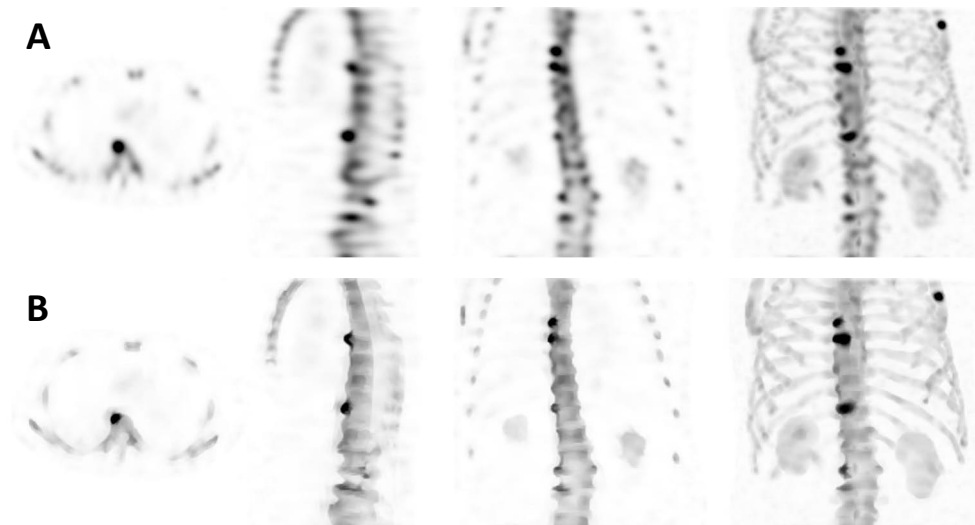


Figure 5. Axial, sagittal, coronal, and maximum intensity projection bone SPECT images of a 65-year-old prostate cancer patient reconstructed using a conventional OSEM algorithm (A) and an anatomically guided algorithm (B).

2.5 Other Modalities for Imaging Bone Metastases

2.5.1 PET-CT

PET is based on a radiopharmaceutical principle quite similar to that of BS and SPECT. However, PET radionuclides do not emit gamma rays by themselves. Instead, they emit positrons, which travel approximately 1 mm in tissue and collide with electrons [187]. In this collision, electron-positron annihilation occurs, and two 511 keV gamma rays are emitted in opposite directions. These gamma-ray pairs are detected during PET acquisition [187].

One of the radionuclides widely used in PET is ^{18}F , which has a physical half-life of 110 min [188]. PET imaging of bone is primarily performed with ^{18}F -labeled NaF [189]. However, bone metastases from prostate cancer are nowadays more often imaged using radiopharmaceuticals based on prostate-specific membrane antigens, as they also accumulate in soft tissue metastases [190]. Image examples corresponding to different radiopharmaceuticals are shown in Figure 6.



Figure 6. Maximum intensity projections of ^{18}F -NaF PET acquired from a 50-year-old breast cancer patient with visible bone metastases in spine, ribs, and pelvis (A) and ^{18}F -PSMA-1007 PET acquired from a 72-year-old prostate cancer patient with visible bone metastases in ribs (B).

A PET-CT system consists of a patient bed, a ring-shaped stationary detector array around the bed, and a CT scanner. No collimator is required, as the annihilation is assumed to be located along the line that connects the two detectors that have recorded coincidence gamma rays [187]. Due to the lack of a physical collimator, the gamma-ray detection efficiency of a PET system is a hundredfold greater than that of a SPECT system [45].

The PET projection data are acquired by the near-simultaneous detection of the gamma-ray pairs emitted from annihilation events. The acquired data are reconstructed using iterative algorithms similar to those used for SPECT. The high temporal resolution of PET detectors allows for time-of-flight measurements, which can be utilized to enhance the reconstruction [191]. Furthermore, PET is a functional imaging modality for which the concept of hybrid imaging is routinely applied, yielding PET-CT images [189].

The diagnostic performance of ^{18}F -NaF PET-CT in bone metastasis detection is very high. In a recent meta-analysis of 12 studies with a total of 507 patients, ^{18}F -NaF PET-CT had a near-perfect patient-level sensitivity of 98% and a high specificity of 90% [192].

2.5.2 CT

Until now, CT has been presented as a complementary examination in the context of hybrid imaging. However, standalone CT is one of the most prevalent tomographic diagnostic tools in terms of frequency of use and hospital availability [193], and imaging of bone and soft tissue metastases is one of its many applications.

The main difference between standalone and complementary CT examinations is the image quality, radiation dose, and use of contrast agent (Figure 7). The image quality is controlled by the X-ray tube current and exposure time. The higher they are, the more X-rays are emitted, and the lower the image noise is. The radiation dose also increases with the tube current and exposure time. Noisier low-dose CT images acquired during SPECT-CT are adequate for attenuation correction, anatomical localization, and, to some extent, anatomical characterization of skeletal findings. However, their utility for soft-tissue characterization is limited. Typical tube current–exposure time products used in SPECT-CT and standalone CT are 2.5–40 mAs and 40–335 mAs, respectively [24].

Intravenously injected contrast agent improves visualization of the target tissue by increasing the attenuation difference between the blood-rich target tissue and the surrounding tissue and fluids [194]. A contrast agent is often required in soft tissue imaging, but for bone imaging, a contrast agent is not usually necessary [57]. Finally, standalone CT employs more advanced technologies, such as the dual-energy method [195].

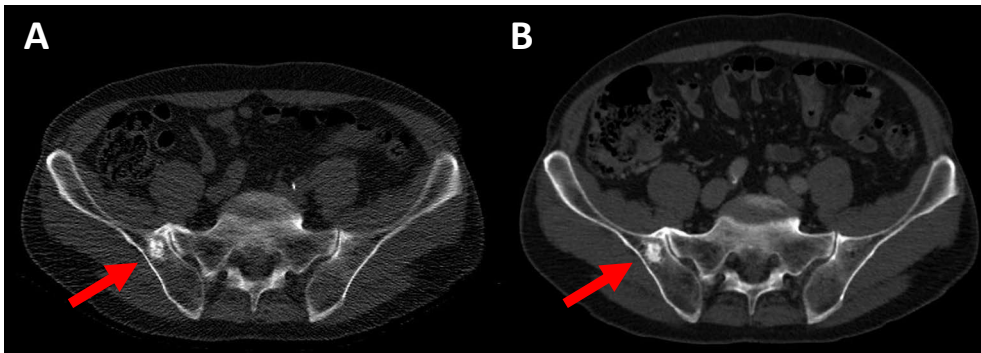


Figure 7. Low-dose (A) and full-dose (B) axial CT images acquired via SPECT-CT and standalone CT, respectively, of the same 72-year-old prostate cancer patient with visible bone metastasis in pelvis.

CT has limited sensitivity but high specificity for bone metastasis detection. In a meta-analysis of 145 studies with a total of 15221 patients, the patient-level sensitivity and specificity of CT were 73 and 95%, respectively [196].

2.5.3 MRI

MRI is based on the magnetization of tissue by an external magnetic field and subsequent excitation of tissue by radio waves. The excited tissue relaxes and emits radio waves, which are collected by receiver coils positioned around the patient. Unlike SPECT, PET, and CT, in which the image reconstruction is based on projections, reconstruction in MRI is based on frequency, amplitude and phase information from the acquired radio waves. That information is converted into an image by Fourier transformation [197, 198].

The main magnetic field of an MRI system is constantly active and has a typical field strength of 1.5 or 3 T. The system also produces weaker gradient fields with strengths up to 45 mT/m [199]. During image acquisition, gradient fields and radio waves are applied in sequences, which define the appearance of an MRI image. Different sequences produce different contrasts between tissues [197, 198].

MRI is primarily used as an anatomical imaging technique. However, functional information can be obtained, for example, by diffusion-weighted imaging, which is based on the diffusion motion of water molecules in tissue [200–202]. In diffusion-weighted images, bone metastases appear with higher intensity compared to surrounding tissue due to restriction of water in bone metastases. DW-MRI combines anatomical and functional diffusion-weighted imaging sequences (Figure 8).

The diagnostic performance of MRI in bone metastasis detection is very high. In a meta-analysis of 145 studies with a total of 15221 patients, the patient-level sensitivity and specificity of MRI were 91 and 95%, respectively [196].

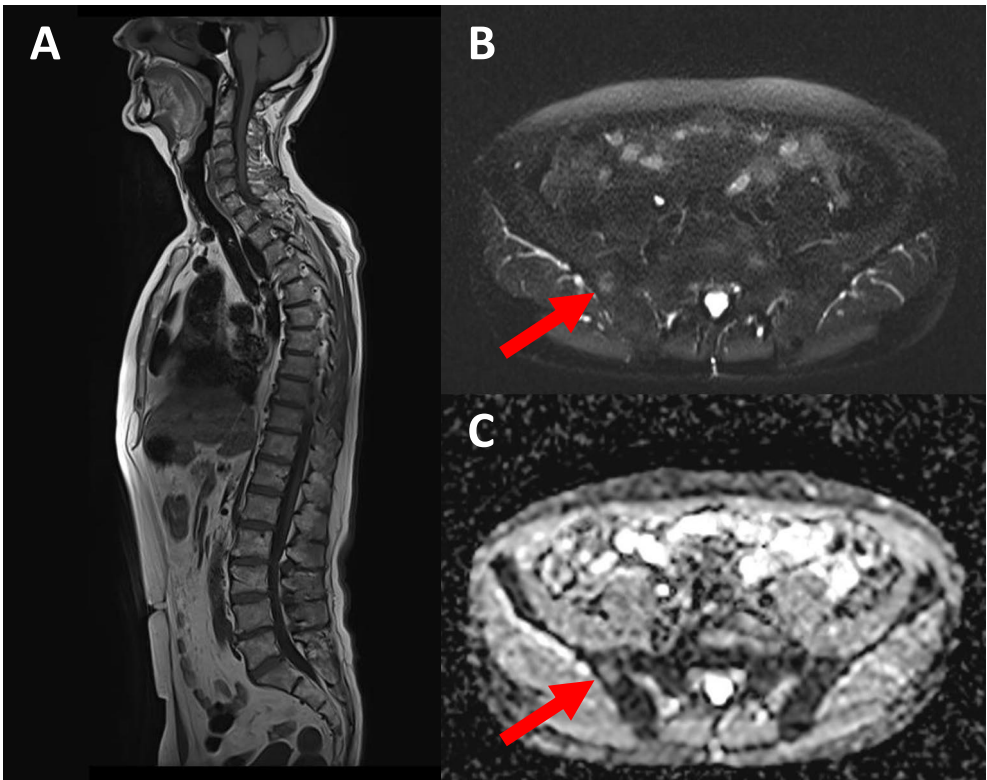


Figure 8. Anatomical sagittal (A), anatomical axial (B), and diffusion-weighted axial (C) MRI images of a 72-year-old prostate cancer patient with visible bone metastasis in pelvis.

3 Aims

This thesis focused on the optimization and validation of the various new methods for the SPECT-CT imaging of bone metastases. The specific aims of Studies I, II, and III were as follows:

- I optimization of bone SPECT acquisition for a CZT system
- II validation of reprojected bone SPECT-CT (RBS) against conventional BS
- III validation of bone SPECT SUVs against bone PET SUVs.

4 Materials & Methods

4.1 Patients and Reference Standard Diagnosis

This thesis is based on retrospective analyses of the patient data acquired during two prospective clinical trials, SKELETA (NCT01339780) and PROSTAGE (NCT03537391), whose primary results have been published by Jambor et al. [19] and Anttinen et al. [20], respectively. All patients included in these trials were considered at high risk for bone metastases. The inclusion criteria consisted of suspicious laboratory findings, suspicious histopathologic findings, and localized pain in the skeletal area suggesting bone metastases.

During these trials, the patients underwent multiple different imaging examinations, including BS, contrast-enhanced CT, SPECT-CT, PET-CT, and DW-MRI. The examinations in each patient were performed within 14 days, and the patients were followed for at least six months. The patient numbers, enrolment dates, and imaging examinations of each trial are listed in Table 1.

Table 1. Patient populations enrolled for SKELETA and PROSTAGE trials, imaging examinations performed during the trials, systems used for BS and SPECT-CT, and the numbers of trial patients included in the studies of this thesis.

Trial name	SKELETA	PROSTAGE
Patients	27 prostate cancer patients 26 breast cancer patients	78 prostate cancer patients
Enrolment date	February 2011 – March 2013	March 2018 – June 2019
Imaging examinations	^{99m} Tc-HDP BS ^{99m} Tc-HDP SPECT-CT ¹⁸ F-NaF PET-CT 1.5-T whole-body DW-MRI	^{99m} Tc-HMDP BS ^{99m} Tc-HMDP SPECT-CT ¹⁸ F-PSMA-1007 PET-CT 1.5-T whole-body DW-MRI Contrast-enhanced CT
SPECT-CT system	Symbia T6	Discovery NM/CT 670 CZT
Patients in Study I	0	30
Patients in Study II	53	78
Patients in Study III	53	0

The malignancy of each imaging finding was defined in regularly organised consensus meetings by a multidisciplinary team, including nuclear medicine physician, radiologist, and oncologist or urologist. Detailed descriptions of image interpretation for the different imaging modalities are given in [19, 20]. The examination results from all primary and follow-up imaging modalities, laboratory results and clinical follow-up data were utilised to determine the reference standard diagnosis. The reference standard diagnoses made for SKELETA and PROSTAGE trials were used as the reference in the studies of this thesis.

4.2 Data Acquisition

BS

The patients received an intravenous injection of 670 MBq of ^{99m}Tc -HDP or HMDP, and BS was started three hours after the injection. The SKELETA patient population was scanned using Symbia T6 system (Siemens Healthineers, Erlangen, Germany) with low-energy high-resolution collimators, continuous acquisition with a scan speed of 13 cm/min and a matrix size of 256×1024 . The PROSTAGE patient population was scanned using Discovery NM/CT 670 CZT system (GE Healthcare, Tirat Hacarmel, Israel) with wide-energy high-resolution collimators, step-and-shoot acquisition, five bed positions, three minutes per bed position, and a matrix size of 256×1024 .

SPECT-CT

A three-bed-position whole-body SPECT was performed from the top of the skull to the middle femurs immediately after BS. The acquisition parameters for the SKELETA patient population were 90 views (180 projections) over 360 degrees, a 9-s acquisition time per view, a 128×128 matrix, and a 15% energy window centered at 140 keV. The acquisition parameters for the PROSTAGE patient population were the same, except for 60 views (120 projections) over 360 degrees with a 13-s acquisition time per view. In PROSTAGE trial, the SPECT data were acquired in list mode. For all patients, the SPECT imaging was followed by a low-dose attenuation-correction CT from the top of the head to the middle femurs.

The systems were calibrated for SUV measurements by imaging uniform cylindrical phantoms. The phantom used for the calibration of Symbia T6 was filled with 6900 ml of water and 141 MBq of ^{99m}Tc -pertechnetate at the time of imaging, resulting in an activity concentration of 20.4 kBq/ml. The phantom used for the calibration of Discovery NM/CT 670 CZT was filled with 6900 ml of water and 126 MBq of ^{99m}Tc -pertechnetate at the time of imaging, resulting in an activity concentration of 18.3 kBq/ml. The calibration images were acquired with the same parameters as the

patient examinations.

4.3 Data Processing

SPECT Resampling

For the optimization of SPECT acquisition in Study I, the originally acquired list-mode data were resampled using Lister software on a Xeleris 4 workstation (GE Healthcare, Haifa, Israel) to produce data sets with either the energy window narrowed from 15 to 10, 8, 6, or 4%, the matrix size increased from 128×128 to 256×256 , or the acquisition time per view reduced from 13 to 10, 9, 7, 5, or 3 s. The idle time including also bed movements in a three-bed-position SPECT was 11 minutes. Therefore, the acquisition times of 13, 10, 9, 7, 5, and 3 s per view correspond to total imaging times of 50, 41, 38, 32, 26, and 20 min, respectively. An additional dataset with 16-min total acquisition time was generated by halving the number of views from 60 to 30 in the images with 5-s acquisition time per view. The number of views was halved using Angular Resampling software on the Xeleris workstation. This reduction in views reduced the idle time from 11 to 8 minutes.

For the validation of RBS in Study II, the acquired SPECT data were resampled such that the number of counts in RBS images was comparable to that of BS images. The data from the Discovery NM/CT 670 CZT system was resampled using the Lister software, and the data from the Symbia T6 system was Poisson resampled using the HybridRecon-Oncology software (version 3.2, HERMES Medical Solutions AB, Stockholm, Sweden).

SPECT Reconstruction

The SPECT data were reconstructed with HybridRecon-Oncology software (versions 1.3, 3.0, and 3.2) using the OSEM algorithm with 6 or 10 iterations, 15 subsets, and corrections for photon attenuation, scatter, and collimator response. A relatively high number of iterations, 10, was used in Study III to increase the quantitation accuracy of SPECT closer to that of PET. Attenuation correction was based on the attenuation coefficient maps derived from the CT images, and scatter correction was performed using a Monte Carlo simulation with 10^5 to 10^6 simulated photons and two scatter update iterations. Collimator response was corrected using Gaussian diffusion model.

The images were filtered using a Gaussian filter with 7-mm FWHM, except during the diagnostic performance analysis in Study I, the FWHM was increased to 10 and 12 mm for the 32- and 26-min images, respectively. The 16-min images in Study I were processed differently to replicate the processing method used in a previous study by Gregoire et al. [25]. Those images were reconstructed with the Evolution

Table 2. Combinations of iterations, subsets, and filters used in the OSEM reconstructions in the different studies.

	Iterations	Subsets	Filter
Study I	6	15	Gaussian 7 mm FWHM
	6	15	Gaussian 10 mm FWHM
	6	15	Gaussian 12 mm FWHM
	3	10	Butterworth 0.48 cycles/cm cutoff, 1.2 order
Study II	6	15	Gaussian 7 mm FWHM
Study III	10	15	Gaussian 7 mm FWHM

for Bone SPECT software on the Xeleris workstation using the OSEM algorithm with 3 iterations and 10 subsets and corrections for photon attenuation and collimator response. A Butterworth postfilter with a cutoff frequency of 0.48 cycles/cm and an order of 1.2 was applied. The combinations of iterations, subsets, and filters used in the different studies are summarized in Table 2.

RBS images corresponding to traditional anterior and posterior views of BS were generated by forward projecting the reconstructed three-bed-position SPECT data. The forward projector of the Hermes HybridRecon reconstruction algorithm traces photons to anterior and posterior detector positions through the CT-based attenuation map used in SPECT reconstruction. The RBS images were filtered using a Gaussian filter with 7-mm FWHM.

The calibration images required for SUV measurements were reconstructed similarly to patient images. From the calibration images, coefficients to convert the reconstructed counts into units of activity concentration were calculated as the ratio between true activity and reconstructed counts in a homogeneous volume of interest (VOI). Voxel SUVs in patient images were then calculated using the equation:

$$\text{SUV} = \frac{cW}{A}, \quad (7)$$

where where c is the activity concentration (Bq/ml), W is the patient body weight (g) converted to volume (ml) assuming a density of 1.0 g/ml, and A is the injected activity (Bq) corrected for decay and syringe residual activity.

4.4 Image Analysis

Qualitative Image Analysis

Qualitative analysis was done in Studies I and II, and it was essentially visual grading of images by experienced nuclear medicine physicians. The physicians evaluated overall image quality and lesion visibility on a five-point Likert-type scale: 1 = insufficient, 2 = almost sufficient, 3 = sufficient, 4 = good, and 5 = excellent image quality for diagnostic use.

The qualitative analysis in Study I was performed in two rounds. The first round included the originally acquired images, images with 10, 8, 6, and 4% energy window widths, and images with a 256×256 matrix from 15 patients. The second round included the originally acquired images and images with 38-, 32-, 26-, and 20-min acquisition times from all 30 patients. All images were evaluated by three physicians. In Study II, only the overall image quality of BS and RBS images was evaluated. The BS and RBS images were evaluated by two pairs of different physicians.

Quantitative Image Analysis

Quantitative image analysis was carried out in all three studies, and it essentially consisted of measurements of SUV, contrast, and noise. In Study I, the quantitative analysis included the originally acquired 50-min images, images with 41-, 32-, 26-, and 20-min acquisition times, images with 10, 8, 6, and 4% energy window widths, and images with 256×256 matrix from all 30 patients. Benign and metastatic lesions were first segmented from the original images using an initial threshold of SUV = 12. The threshold was lowered if the resulting VOI was, by visual evaluation, clearly smaller than the area of high uptake. The threshold was increased if another high-uptake area was nearby. The same threshold value was used for the same lesion in different images.

From the resulting VOIs, lesion maximum, peak, and mean SUVs (SUV_{max} , SUV_{peak} , SUV_{mean}) and volume were measured. SUV_{max} was determined as the SUV of the most active voxel within the VOI, SUV_{peak} as the average SUV of 1-cm^3 cube positioned within the lesion such that the enclosed average SUV was maximized, and SUV_{mean} as the average SUV of the whole VOI.

In addition, 5-10 circular regions of interest (ROIs) with a 1-cm diameter were drawn on normal appearing bone adjacent to the lesion. These ROIs were summed to form the background VOI, whose mean SUV ($SUV_{mean, bg}$) and standard deviation (SD) of SUV ($SUV_{SD, bg}$) were defined. Contrast was then calculated by dividing the difference between SUV_{mean} and $SUV_{mean, bg}$ by $SUV_{mean, bg}$, noise by dividing $SUV_{SD, bg}$ by $SUV_{mean, bg}$, and the contrast-to-noise ratio (CNR) by dividing contrast by noise.

In Study II, the quantitative quality of BS and RBS images was measured in a randomly chosen sample of 20 patients. Circular ROIs with 15-mm diameter were placed in BS and RBS images on a normal appearing femur, lumbar vertebra, the tenth rib, and adjacent soft tissue. Mean and SD of counts in bone and soft tissue ROIs were defined, and CNRs were calculated as:

$$\text{CNR} = \frac{\text{ROI}_{\text{bone, mean}} - \text{ROI}_{\text{soft tissue, mean}}}{\sqrt{\text{ROI}_{\text{bone, SD}}^2 + \text{ROI}_{\text{soft tissue, SD}}^2}}, \quad (8)$$

where $\text{ROI}_{\text{bone, mean}}$ and $\text{ROI}_{\text{soft tissue, mean}}$ are means of counts and $\text{ROI}_{\text{bone, SD}}^2$ and $\text{ROI}_{\text{soft tissue, SD}}^2$ are squared SDs of counts in bone and soft tissue ROIs, respectively.

In Study III, skeletal lesions visible in both SPECT and PET images were first segmented from PET images using a threshold of $\text{SUV} = 15$, which was lowered if the resulting VOI was clearly smaller than the area of increased uptake. Next, the same lesions were segmented from SPECT images using SUV thresholds that resulted in VOIs with the volumes similar to those in PET images. SUV_{max} , SUV_{peak} , SUV_{mean} , and $\text{SUV}_{\text{mean, bg}}$ were then measured as in Study I. Maximum, peak, and mean SUV ratios (SUVR_{max} , $\text{SUVR}_{\text{peak}}$, $\text{SUVR}_{\text{mean}}$) of the lesions were calculated by dividing the SUV_{max} , SUV_{peak} , and SUV_{mean} of the lesion by the corresponding $\text{SUV}_{\text{mean, bg}}$.

Diagnostic Performance Analysis

Diagnostic performance analysis was done in Studies I and II, and it was essentially measurements on how experienced nuclear medicine physicians detect bone metastases from images. In Study I, the diagnostic performance analysis included the original 50-min SPECT images and the specially processed 32-, 26-, and 16-min images of all 30 patients. Lesions suggestive for bone metastases were reported from the fused SPECT-CT images by two physicians. In Study II, all BS and RBS images were double read by two pairs of physicians. The physicians worked independently and were blinded to the results of the other imaging modalities. They were only informed that the patients had breast or prostate cancer at high risk for bone metastases.

A lesion was marked equivocal if the reading physician was not sure whether to report it or not. In Study I, the reports given by the physicians were analyzed in a pessimistic manner, such that equivocal lesions were considered bone metastases. In Study II, the pessimistic analysis was complemented by optimistic analysis, where the equivocal lesions were omitted. To create true positive, true negative, false positive and false negative classes, the reported lesions were validated against the reference standard diagnosis, which was created during the SKELETA and PROSTAGE trials.

The diagnostic performance of different images was compared at the patient, region, and lesion levels. In the region-level analysis, the skeleton was divided into six segments: skull, spine, ribs, pectoral girdle and sternum, pelvis, and limbs.

4.5 Statistical Analysis

Statistical analyses were performed using MedCalc statistical software (version 19.2.6, MedCalc Software Ltd, Ostend, Belgium). Lesion visibility and overall image quality scores given by the readers were pooled, reported using the mean and SD, and compared using the Wilcoxon signed-rank test. Lesion visibility and overall image quality failure rates represent the percentage of images rated 1 or 2, i.e., qualitatively not sufficient for diagnostic use. The failure rates were compared using the $N - 1$ chi-squared test.

The median, percentiles, and interquartile range (IQR) are used to describe non-normally distributed quantitative measurements. Scatter plots and linear regression models were used to evaluate the correlations between SUVs and SUVRs of SPECT and PET data, and Bland–Altman plots were created to evaluate the agreements between them. In Bland–Altman plots, the mean difference and 95% limits of agreement (LOA) were estimated using the median and the 2.5th and 97.5th percentiles of the differences because the differences were not normally distributed. The Wilcoxon signed-rank test was used to determine whether the SUVs and SUVRs of SPECT and PET were statistically different.

Diagnostic performance was evaluated in terms of sensitivity, specificity, accuracy, and area under the receiver-operating characteristic curve (AUC). The sensitivity, specificity, and accuracy were compared between different images at the patient and region levels using the McNemar test and Fisher's exact test. The AUC values were calculated using the trapezoid rule and compared using the method of Hanley and McNeil. The diagnostic performance values are reported with a 95% confidence interval ($CI_{95\%}$). P values < 0.05 were considered statistically significant.

5 Results

5.1 Optimal Acquisition of Bone SPECT Using a CZT System

In the qualitative analysis, the original images scored best in terms of both lesion visibility and image quality. However, the energy window could be narrowed to 8%, the acquisition time reduced to 38 min, or the matrix size increased to 256×256 without significantly affecting lesion visibility or image quality failure rates. The given scores for lesion visibility and overall image quality in different images and their corresponding failure rates are summarized in Table 3.

Table 3. Scores and failure rates for lesion visibility and image quality with different acquisition parameters (from original publication I).

Acquisition time	Energy window	Matrix size	N	Lesion visibility score, mean (SD)	Image quality score, mean (SD)	Lesion visibility failure rate	Image quality failure rate
50 min	15%	128×128	45	3.8 (0.8)	3.6 (0.9)	4%	11%
50 min	10%	128×128	45	3.8 (0.9)	3.5 (1.0)	4%	16%
50 min	8%	128×128	45	3.7 (1.0)	3.4 (1.1)	11%	27%
50 min	6%	128×128	45	3.6 (0.9)	3.1 (1.0) ^a	9%	31% ^a
50 min	4%	128×128	45	3.5 (0.9) ^a	2.7 (1.1) ^a	7%	49% ^a
50 min	15%	256×256	45	3.7 (0.9)	3.3 (1.0) ^a	7%	22%
50 min	15%	128×128	90	4.2 (0.8)	3.8 (1.0)	0%	13%
38 min	15%	128×128	90	3.8 (0.8) ^b	3.4 (1.0) ^b	2%	19%
32 min	15%	128×128	90	3.4 (0.9) ^b	2.9 (1.0) ^b	11% ^b	37% ^b
26 min	15%	128×128	90	3.0 (1.0) ^b	2.2 (1.0) ^b	32% ^b	67% ^b
20 min	15%	128×128	90	2.3 (1.0) ^b	1.4 (0.6) ^b	58% ^b	92% ^b

N = Total number of scores, i.e., the number of readers multiplied by the number of images.

^a Statistically significant difference ($p < 0.05$) compared with original images ($N = 45$).

^b Statistically significant difference ($p < 0.05$) compared with original images ($N = 90$).

The quantitative analysis was performed in 130 lesions. Generally, SUV measures and lesion volumes were not affected by changes in energy window width, matrix size or acquisition time per view. The only exception was noticeably low SUV_{peak} in images with 256×256 matrix size, as the median difference was -13% with respect to original images. The median differences for other measures and images ranged from -4 to 2%. Acquisition time shortening, energy window narrowing, and 256×256 image matrix all increased contrast slightly but less than they increased noise, resulting in decreased CNR (Table 4).

Table 4. Contrast, noise, and CNR of images with different acquisition parameters (modified from original publication I).

Acquisition time	Energy window	Matrix size	Contrast, median (IQR)	Noise, median (IQR)	CNR, median (IQR)
50 min	15%	128×128	2.0 (1.4–3.2)	0.09 (0.08–0.11)	22.2 (15.7–31.1)
50 min	10%	128×128	2.0 (1.4–3.4)	0.12 (0.09–0.16)	17.5 (12.0–24.3)
50 min	8%	128×128	2.1 (1.4–3.5)	0.13 (0.10–0.18)	17.4 (12.6–25.8)
50 min	6%	128×128	2.2 (1.4–3.5)	0.15 (0.12–0.18)	14.4 (10.4–21.3)
50 min	4%	128×128	2.3 (1.4–3.6)	0.18 (0.15–0.22)	12.8 (8.2–20.1)
50 min	15%	256×256	2.1 (1.4–3.2)	0.12 (0.10–0.15)	17.1 (12.1–24.5)
41 min	15%	128×128	2.0 (1.4–3.3)	0.12 (0.10–0.16)	18.0 (12.0–25.8)
32 min	15%	128×128	2.1 (1.4–3.3)	0.15 (0.11–0.19)	14.0 (9.4–20.3)
26 min	15%	128×128	2.1 (1.4–3.3)	0.17 (0.14–0.23)	12.7 (8.3–19.7)
20 min	15%	128×128	2.2 (1.5–3.6)	0.22 (0.18–0.29)	10.8 (7.1–15.3)

According to the reference standard diagnosis, 12 patients out of 30 had bone metastases, 35 different skeletal regions contained bone metastases, and altogether 100 lesions were considered positive for bone metastases. Acquisition time reduction had little effect on the diagnostic performance, as sensitivity, specificity, accuracy, and AUC were not significantly different between the 50-min total acquisition time and reduced acquisition time images. The number of equivocal lesions tended to increase as the acquisition time decreased. The results of the patient-, region-, and lesion-level analyses with decreasing acquisition time are given in Tables 5–7. Examples of images with different acquisition times and filters are shown in Figure 9.

Table 5. Patient-level analysis with decreasing acquisition time (from original publication I).

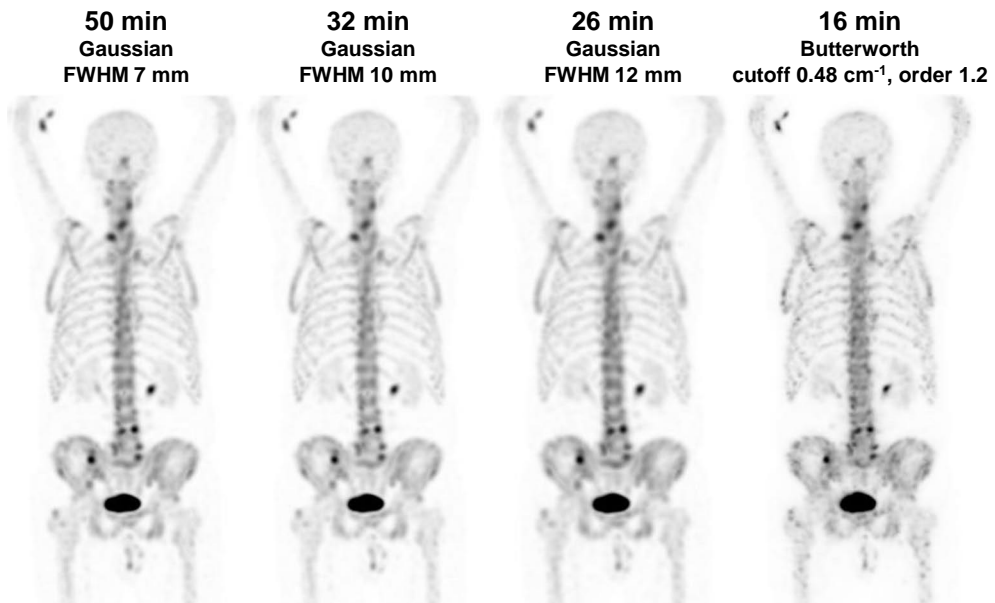
	Acquisition time	Sensitivity (CI _{95%})	Specificity (CI _{95%})	Accuracy (CI _{95%})	AUC (CI _{95%})
Reader A	50 min	83% (52–98%)	83% (59–96%)	83% (65–94%)	0.83 (0.65–0.94)
	32 min	83% (52–98%)	78% (52–94%)	80% (61–92%)	0.81 (0.62–0.93)
	26 min	100% (74–100%)	78% (52–94%)	87% (69–96%)	0.89 (0.72–0.97)
	16 min	100% (74–100%)	72% (47–90%)	83% (65–94%)	0.86 (0.69–0.96)
Reader B	50 min	92% (62–100%)	72% (47–90%)	80% (61–92%)	0.82 (0.64–0.94)
	32 min	100% (74–100%)	89% (65–99%)	93% (78–99%)	0.94 (0.80–1.00)
	26 min	100% (74–100%)	89% (65–99%)	93% (78–99%)	0.94 (0.80–1.00)
	16 min	92% (62–100%)	83% (59–96%)	87% (69–96%)	0.88 (0.70–0.97)

Table 6. Region-level analysis with decreasing acquisition time (from original publication I).

	Acquisition time	Sensitivity (CI _{95%})	Specificity (CI _{95%})	Accuracy (CI _{95%})	AUC (CI _{95%})
Reader A	50 min	57% (39–74%)	96% (91–98%)	88% (83–93%)	0.77 (0.70–0.83)
	32 min	57% (39–74%)	97% (92–99%)	89% (83–93%)	0.77 (0.70–0.83)
	26 min	63% (45–79%)	94% (89–98%)	88% (83–93%)	0.79 (0.72–0.84)
	16 min	57% (39–74%)	91% (85–95%)	84% (78–89%)	0.74 (0.67–0.80)
Reader B	50 min	53% (36–69%)	94% (88–97%)	85% (79–90%)	0.77 (0.70–0.83)
	32 min	58% (41–74%)	98% (94–100%)	89% (84–94%)	0.80 (0.74–0.86)
	26 min	55% (38–71%)	98% (94–100%)	89% (84–93%)	0.79 (0.72–0.85)
	16 min	55% (38–71%)	98% (94–100%)	89% (83–93%)	0.79 (0.72–0.85)

Table 7. Lesion-level analysis with decreasing acquisition time (from original publication I).

	Acquisition time	Number of positive lesions reported	Number of true positive lesions	Number of false positive lesions	Number of false negative lesions	Number of equivocal lesions reported	Ratio of equivocal to all detected lesions
Reader A	50 min	52	49	3	51	11	17%
	32 min	40	36	4	64	14	26%
	26 min	37	35	2	65	17	31%
	16 min	49	43	6	57	26	35%
Reader B	50 min	55	52	3	48	7	11%
	32 min	54	53	1	47	5	8%
	26 min	51	49	2	51	3	6%
	16 min	52	50	2	50	4	7%
Total	50 min	107	101	6	99	18	14%
	32 min	93	89	5	111	19	17%
	26 min	88	84	4	116	20	19%
	16 min	101	93	8	107	30	23%

**Figure 9.** Whole-body ^{99m}Tc -HMDP SPECT maximum intensity projections of a 72-year-old prostate cancer patient with different acquisition times and postprocessing filters. The 50-, 32-, and 26-min images are filtered using Gaussian filters with FWHMs of 7, 10, and 12 mm, respectively, and the 16-min image is filtered using a Butterworth filter with a cutoff frequency of 0.48 cycles/cm and an order of 1.2 (modified from original publication I).

5.2 Validation of RBS

A visual comparison of BS and RBS images is shown in Figure. 10. The mean (SD) image quality grades given by the readers were 3.5 (0.7) for BS and 2.3 (0.6) for RBS. The CNR values measured from the femur, lumbar vertebra, and the tenth rib were on average 175, 114, and 185 % higher in RBS images than BS images, respectively.

A total of 34 patients out of 131 had skeletal metastases according to the reference standard diagnosis, 103 different skeletal regions contained bone metastases, and altogether 265 lesions were considered as positive for bone metastases. The optimistic analysis revealed little difference between the diagnostic performance of BS and RBS, while the pessimistic analysis showed RBS to be a more sensitive but less specific method than BS (Tables 8 and 9).

The number of true positive lesions was similar between BS and RBS, but false positive and equivocal lesions were more numerous in RBS images. The numbers of malignant and equivocal lesions reported by each reader and their concordance with the reference standard diagnosis are shown in Table 10.

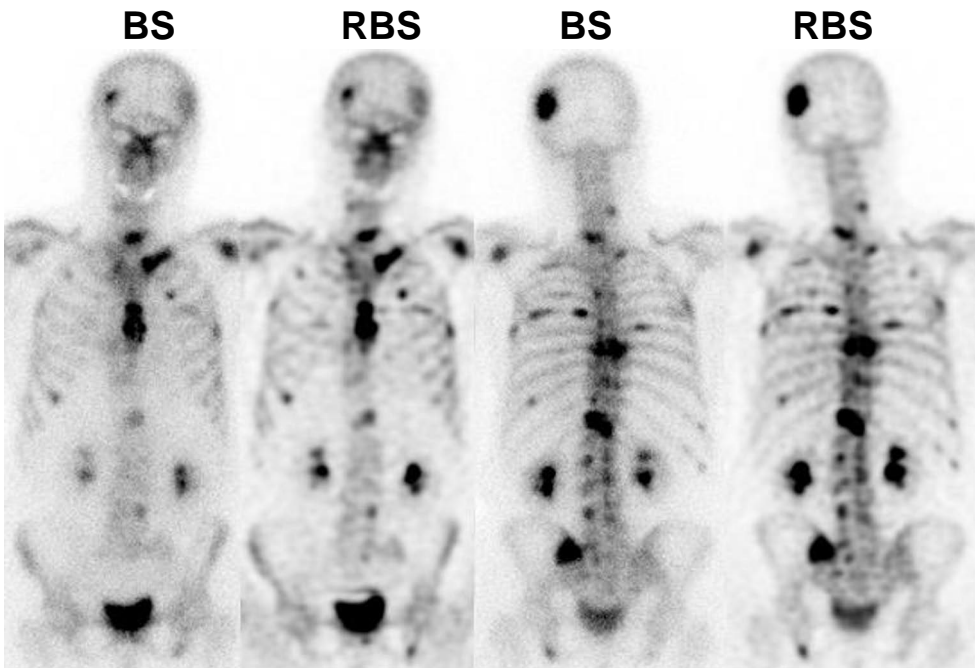


Figure 10. Anterior and posterior views of BS and RBS of a 75-year-old breast cancer patient with widespread bone metastases (from original publication II).

Table 8. Patient-level analysis (from original publication II).

Optimistic analysis				
	Sensitivity (CI _{95%})	Specificity (CI _{95%})	Accuracy (CI _{95%})	AUC (CI _{95%})
BS 1	53% (35–70%)	99% (94–100%)	87% (80–92%)	0.76 (0.68–0.83)
BS 2	62% (44–78%)	97% (91–99%)	88% (81–93%)	0.79 (0.71–0.86)
RBS 1	65% (46–80%)	92% (84–96%) ^a	85% (77–90%)	0.78 (0.70–0.85)
RBS 2	62% (44–78%)	93% (86–97%)	85% (77–90%)	0.77 (0.69–0.84)
Pessimistic analysis				
	Sensitivity (CI _{95%})	Specificity (CI _{95%})	Accuracy (CI _{95%})	AUC (CI _{95%})
BS 1	71% (53–85%)	82% (73–89%)	79% (71–86%)	0.77 (0.68–0.84)
BS 2	79% (62–91%)	75% (65–83%)	76% (68–83%)	0.77 (0.69–0.84)
RBS 1	85% (69–95%)	47% (37–58%) ^{a, b}	57% (48–66%)	0.66 (0.58–0.74) ^b
RBS 2	88% (73–97%) ^a	30% (21–40%) ^{a, b}	45% (36–54%)	0.59 (0.50–0.68) ^{a, b}

BS 1 = bone scintigraphy reader 1; BS 2 = bone scintigraphy reader 2;

RBS 1 = reprojected bone SPECT-CT reader 1; RBS 2 = reprojected bone SPECT-CT reader 2.

^a Statistically significant difference ($p < 0.05$) compared with BS 1.

^b Statistically significant difference ($p < 0.05$) compared with BS 2.

Table 9. Region-level analysis (from original publication II).

Optimistic analysis				
	Sensitivity (CI _{95%})	Specificity (CI _{95%})	Accuracy (CI _{95%})	AUC (CI _{95%})
BS 1	49% (39–59%)	100% (99–100%)	93% (91–95%)	0.74 (0.71–0.77)
BS 2	54% (44–64%)	99% (98–100%)	93% (91–95%)	0.77 (0.74–0.80)
RBS 1	50% (40–60%)	98% (97–99%) ^a	92% (90–94%)	0.74 (0.71–0.77)
RBS 2	46% (36–56%)	98% (97–99%) ^{a, b}	91% (89–93%)	0.72 (0.69–0.75)
Pessimistic analysis				
	Sensitivity (CI _{95%})	Specificity (CI _{95%})	Accuracy (CI _{95%})	AUC (CI _{95%})
BS 1	61% (51–71%)	97% (96–98%)	92% (90–94%)	0.79 (0.76–0.82)
BS 2	66% (56–75%)	94% (92–95%)	90% (88–92%)	0.80 (0.77–0.83)
RBS 1	70% (60–79%) ^a	89% (86–91%) ^{a, b}	86% (84–88%)	0.79 (0.76–0.82)
RBS 2	68% (58–77%)	84% (81–87%) ^{a, b}	82% (79–85%)	0.76 (0.73–0.79)

BS 1 = bone scintigraphy reader 1; BS 2 = bone scintigraphy reader 2;

RBS 1 = reprojected bone SPECT-CT reader 1; RBS 2 = reprojected bone SPECT-CT reader 2.

^a Statistically significant difference ($p < 0.05$) compared with BS 1.

^b Statistically significant difference ($p < 0.05$) compared with BS 2.

Table 10. Lesion-level analysis (from original publication II).

	Number of positive lesions reported	Number of true positive lesions	Detection rate of true positive lesions	Number of false positive lesions	Number of false negative lesions	Number of equivocal lesions reported	Ratio of equivocal to all detected lesions
BS 1	135	134	51%	1	131	43	24%
BS 2	176	169	64%	7	96	62	26%
RBS 1	163	144	54%	19	121	139	46%
RBS 2	163	137	52%	26	128	185	53%

BS 1 = bone scintigraphy reader 1; BS 2 = bone scintigraphy reader 2;

RBS 1 = reprojected bone SPECT reader 1; RBS 2 = reprojected bone SPECT reader 2.

5.3 Validation of Bone SPECT SUVs

A total of 231 skeletal lesions, 129 metastatic and 102 benign, were analyzed. The scatter and Bland–Altman plots for SUV measures are shown in Figure 11. The correlations between SPECT and PET SUVs are strong and statistically significant ($R^2 \geq 0.80$, $p < 0.001$). PET SUVs are significantly higher than SPECT SUVs ($p < 0.001$), and SUV_{peak} is the measure with the smallest difference between SPECT and PET. Metastatic lesions have generally higher SUVs than benign lesions, but the SUV distributions of benign and metastatic lesions overlap greatly.

The scatter and Bland–Altman plots for SUVR measures are shown in Figure 12. The correlations between SPECT and PET SUVRs are slightly weaker than the correlations between their SUVs. However, the SUVRs of SPECT and PET are more similar than their SUVs because PET images have higher background SUVs (Table 11). Only $SUVR_{\text{peak}}$ are significantly different between SPECT and PET. The SUVR distributions of benign and metastatic lesions overlap like the corresponding SUV distributions. Figure 13 contains a visual comparison of SPECT and PET SUV images.

Table 11. $SUV_{\text{mean, bg}}$ from normal appearing bone at different skeletal sites (modified from original publication III).

Skeletal site	PET SUV, median (IQR)	SPECT SUV, median (IQR)	PET SUV – SPECT SUV, median (IQR)
Skull	2.6 (2.1–5.0)	2.0 (1.8–2.6)	0.3 (0.1–0.8)
Spine	7.4 (6.6–8.7)	6.1 (4.7–6.8)	1.7 (0.6–2.8)
Rib cage	3.0 (2.4–4.0)	2.5 (2.0–3.1)	0.7 (-0.1–1.0)
Pelvis	5.5 (4.7–6.6)	4.7 (4.1–6.0)	0.6 (-0.2–1.3)
Limbs	3.8 (2.9–4.9)	3.2 (2.1–4.3)	0.7 (0.1–1.0)

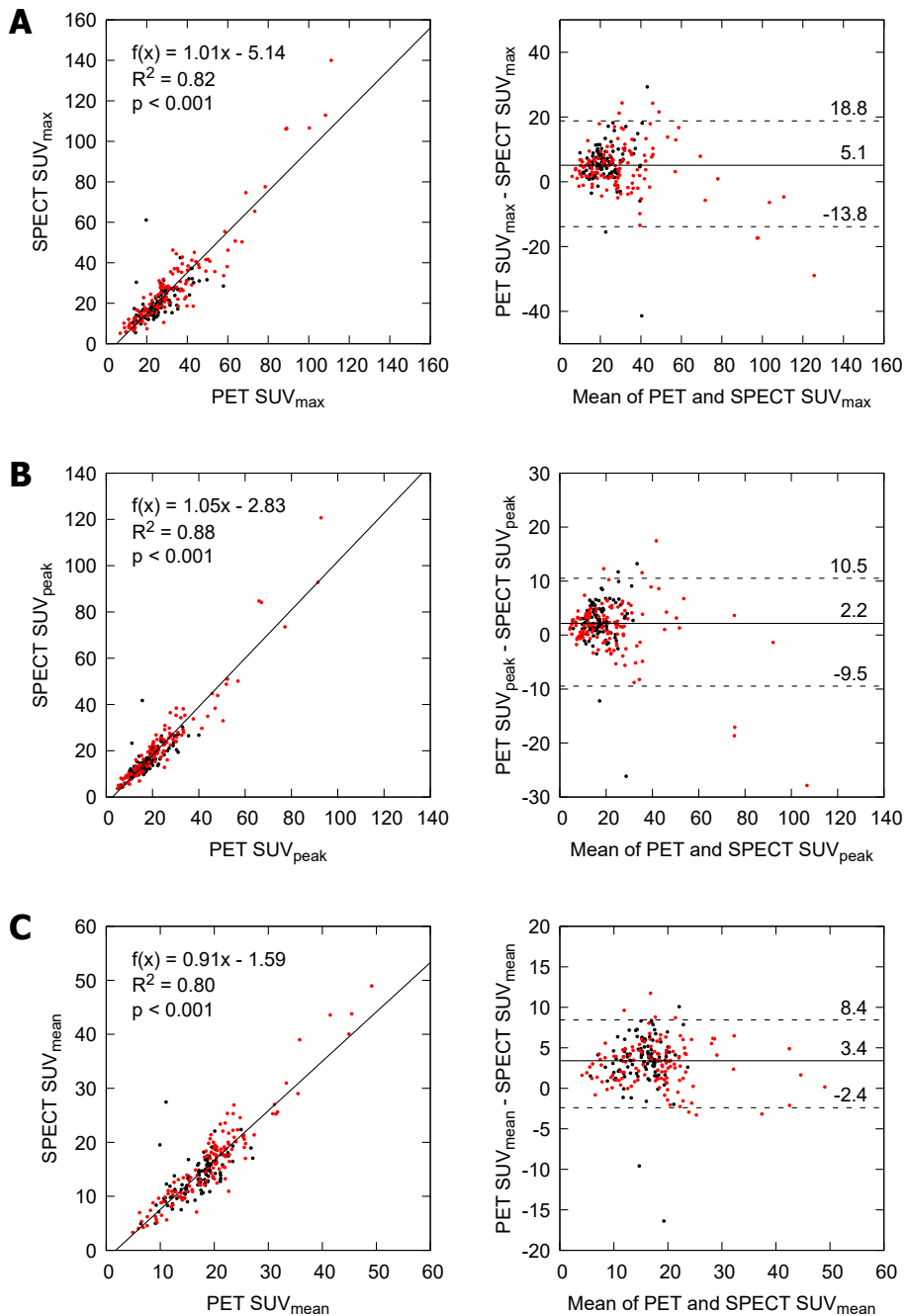


Figure 11. Scatter and Bland–Altman plots for (A) SUV_{max} , (B) SUV_{peak} , and (C) SUV_{mean} of lesions in SPECT and PET images. Metastatic lesions are marked in red and benign in black. In the scatter plots, the regression lines with slopes, y-intercepts and coefficients of determination (R^2) have been calculated using the method of least squares. In the Bland–Altman plots, the solid lines with numerical values denote median differences and the dotted lines denote 95% LOA (modified from original publication III).

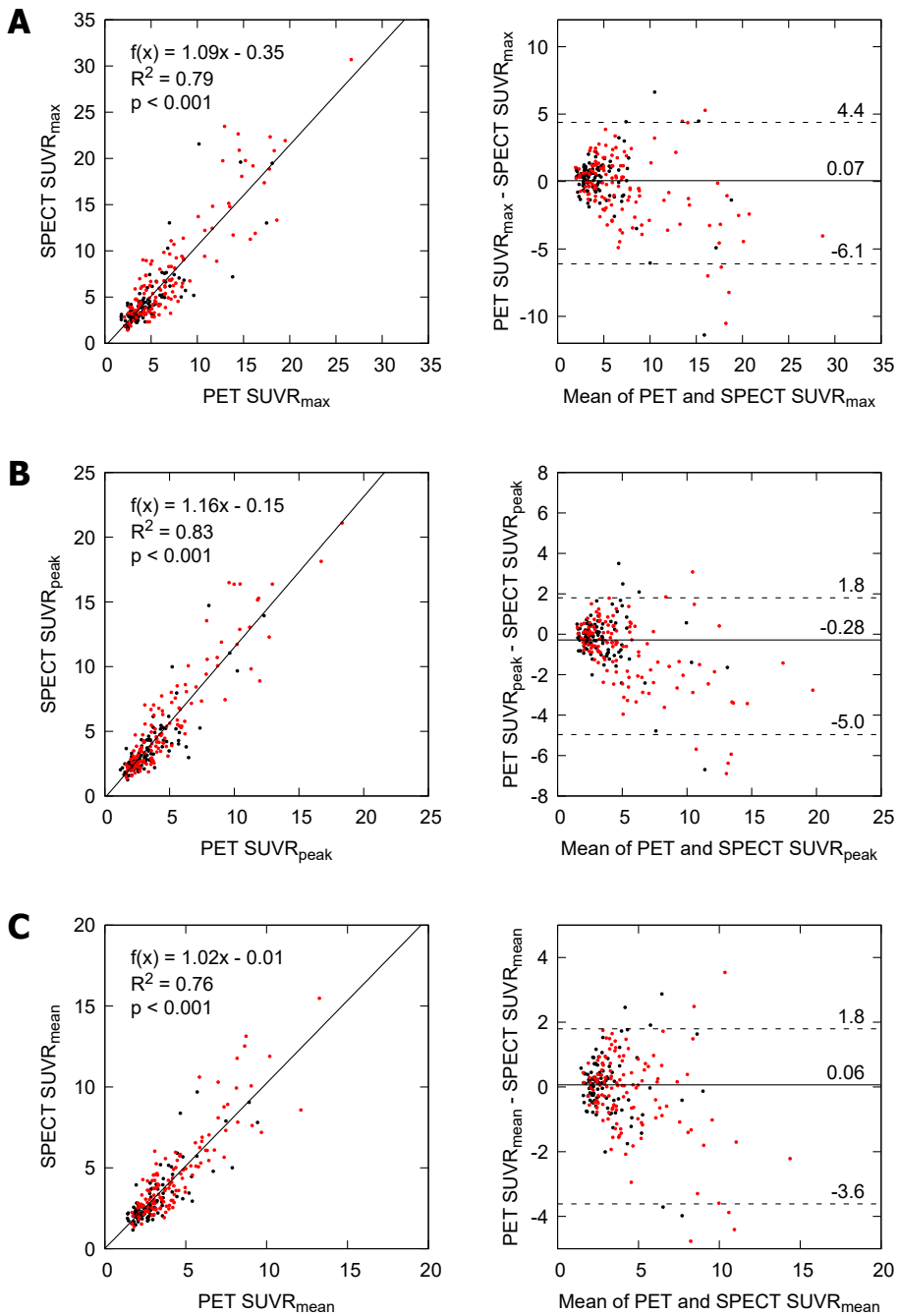


Figure 12. Scatter and Bland–Altman plots for (A) $SUVR_{max}$, (B) $SUVR_{peak}$, and (C) $SUVR_{mean}$ of lesions in SPECT and PET images. Metastatic lesions are marked in red and benign in black. In the scatter plots, the regression lines with slopes, y-intercepts and coefficients of determination (R^2) have been calculated using the method of least squares. In the Bland–Altman plots, the solid lines with numerical values denote median differences and the dotted lines denote 95% LOA (modified from original publication III).

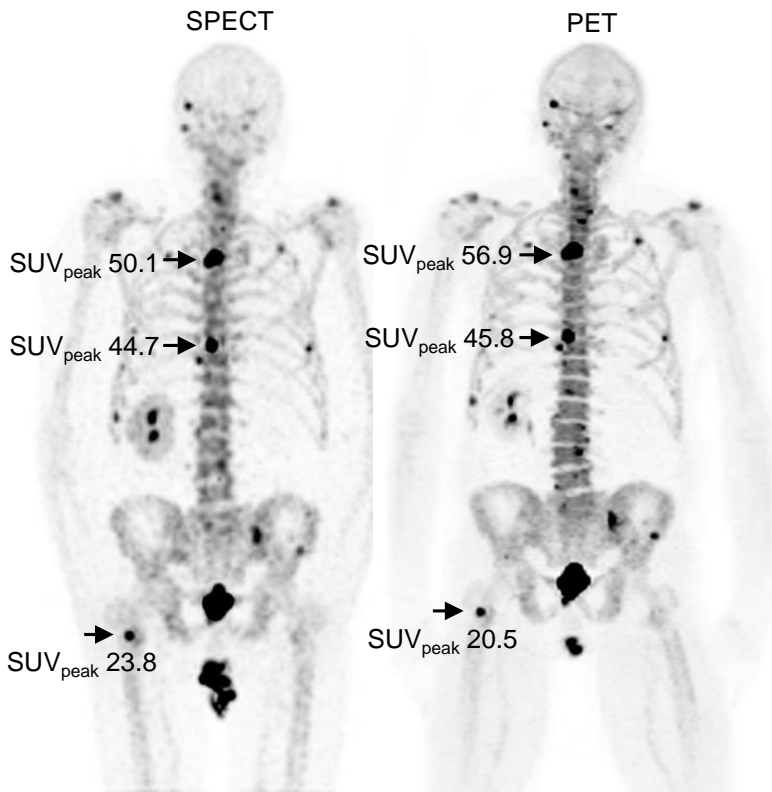


Figure 13. Maximum intensity projections of ^{99m}Tc -HDP SPECT and ^{18}F -NaF PET acquired from the same 66-year-old prostate cancer patient. SUV_{peak} are shown for the most active lesions. The SPECT was acquired two days before the PET (from original publication III).

6 Discussion

The routine method for skeletal imaging in nuclear medicine is expected to shift from planar BS to whole-body bone SPECT-CT [10, 23]. To support this transition, this thesis evaluated whole-body bone SPECT-CT with fast acquisition, reprojection to conventional planar images, and quantitation. Study I shows that whole-body bone SPECT-CT can be acquired in 20 min without compromising diagnostic performance, Study II that planar images reprojected from SPECT-CT perform similarly to acquired BS images in the detection of bone metastases, and Study III that the quantitation accuracy of bone SPECT-CT is comparable to that of bone PET-CT.

6.1 Implications for Routine Clinical Practice

Planar BS has been the routine method for the detection of bone metastases in breast and prostate cancer patients for several decades [11–15]. BS has high sensitivity for bone metastasis detection, but the specificity is rather limited [12, 16, 17]. A separate CT examination has been frequently used to compensate for this low specificity [18]. However, the co-registration between 2D BS and 3D CT can often be challenging due to the lack of exact anatomical localization in BS. Integrated SPECT-CT systems allow for exact anatomical localization, and they have been available for two decades now [10]. The continuing development of technology and expertise in SPECT-CT, combined with superior diagnostic accuracy, are making it a favorable alternative to planar BS.

However, the use of bone SPECT-CT has been generally limited to partial-body imaging as an add-on to whole-body planar BS [23]. The widespread adoption of whole-body bone SPECT-CT has been hindered by the lengthy acquisition and more laborious image reporting. Currently, the acquisition time for whole-body SPECT-CT examinations is typically more than 40 min, and for BS, it is approximately 15 min [24]. With the short acquisition time of 20 min, the clinical use of whole-body bone SPECT-CT could potentially increase significantly.

Some nuclear medicine physicians may still feel reluctant to switch to the more complex and time-consuming reading of multi-slice whole-body SPECT-CT and abandon the familiar methodology of BS. The acquisition of both BS and whole-body SPECT-CT in a row during this transition period might be tempting, but it would greatly increase the examination time. By utilizing RBS images, nuclear

medicine physicians would be provided with a more familiar planar image along with the tomographic image for interpretation without the need for additional scanning.

Breast and prostate cancer patients are commonly examined multiple times for follow-up over several years to evaluate disease progression or treatment response [203]. During the transition from routine planar BS to whole-body bone SPECT-CT, the comparison between previous BS and follow-up SPECT-CT examinations might be challenging due to different image types. However, the comparison between previous BS and follow-up RBS would be more straightforward. Additionally, SPECT-CT would then provide a more comprehensive view of the current state of the disease and a reference for upcoming follow-up SPECT-CT.

SPECT has conventionally been used in a non-quantitative manner, i.e., the images have been visually interpreted using color scale intensities instead of numeric values of radiopharmaceutical uptake [32, 33]. The quantitation by SUVs could complement the visual image analysis in multiple ways. The first application would be longitudinal disease assessment by measuring changes in bone metastasis SUVs between previous and follow-up images [146, 164–167]. An increase in SUV might indicate disease progression, while a decrease might indicate treatment response.

The second application would be the overall standardization of SPECT results between patients, imaging systems and clinical centres [46, 204]. This would be useful in large clinical trials where hundreds of patients are recruited from multiple clinical centres with different imaging systems. SUV measurements would also decrease the interobserver variability in the interpretation of SPECT [146].

The third application would be the automatic normalization of the image intensity scale in visual evaluation [176]. Currently, the intensity scale is initially normalized with respect to the voxel with the highest uptake, which usually represents the bladder. The intensity scale is then manually adjusted such that normal skeletal structures appear with typical intensity. This manual adjustment is required because the magnitude of the highest uptake varies greatly. By using the SUV scale, the typical appearance could be achieved automatically by normalizing to a specific SUV level, for example, $SUV = 15$, as was done in Figures 9 and 13 (pages 45 and 51).

Normalization by SUV would also trivialize the detection of so-called superscans, in which most of the skeleton presents markedly increased activity [12, 176]. This uniformly increased activity may go undetected in visual analyses based on relative activity levels, although reduced activity in kidneys and bladder has been used as a sign of superscan [205].

The main obstacle in the transition from planar BS to whole-body bone SPECT-CT is the increased complexity in the whole examination process. Thus, an immediate adoption of all the presented methods, fast whole-body acquisition, RBS, and SUVs, cannot be expected. Instead, fast whole-body bone SPECT-CT with RBS will probably be the first step, followed by the later adoption of SUVs when the whole-

body bone SPECT-CT examination has become a routine modality.

It should also be kept in mind that while bone PET-CT is a slightly better method in terms of diagnostic performance and routine quantitation, the cost of bone PET-CT is 3- to 4-fold that of bone SPECT-CT [19]. Bone SPECT-CT is therefore the more cost-effective modality for the evaluation of metastatic bone uptake in breast and prostate cancer.

6.2 Reliability and Validity of the Results

In Study I, the diagnostic performance of bone SPECT-CT with reduced acquisition time was evaluated from the fused SPECT-CT images, which corresponds to the current routine procedure in clinical practice. In contrast, the qualitative analyses in Study I were performed by viewing whole-body SPECT without CT, which is nowadays a rare situation. In Study II, the BS and RBS images were evaluated in a manner representing clinical practice, but the more detailed appearance of RBS was unfamiliar to the reading physicians.

All qualitative image analyses are always reader-dependent, as the visual image quality grades given by the reading physicians reflect the image quality to which they are accustomed. Quantitative analyses are more reliable, although their results can be affected by image processing conditions and VOI definition.

For now, Study I seems to be the only published receiver-operating characteristic analysis comparing whole-body bone SPECT-CT with different acquisition times. However, qualitative analysis of fast bone SPECT has been published before by Gregoire et al. [25]. They concluded that images similar to the 16-min images presented in Study I are sufficient for diagnostic use. Additionally, quantitative analysis of fast bone SPECT has been published before by Yamane et al. [206]. They focused mainly on SUV_{max} and concluded that images also similar to the 16-min images are acceptable for the clinical evaluation of quantitative values.

Little evidence of RBS exists in the literature, and so far, Study II appears to be the only published study evaluating the diagnostic performance of RBS. The RBS method has been presented earlier [26], but the usage of reprojected SPECT has been previously validated only for lung [134–137] and gated blood-pool imaging [138, 139]. The results of SUV comparison between bone SPECT-CT and PET-CT in Study III have been recently confirmed by Tanaka et al. [207]. However, they reported slightly weaker correlations between SPECT-CT and PET-CT, probably due to differences in image processing.

All patients underwent PET-CT and DW-MRI imaging in addition to BS and SPECT-CT. In addition to consensus reading of all imaging modalities, clinical, and imaging follow-up of at least six months were used to define true nature of the lesions detected by each of the modalities. This approach is similar to other studies focusing on the detection of bone metastases [27, 124]. All readers were highly experienced

nuclear medicine physicians or radiologists with at least five years of experience in the detection of bone metastases using their specific imaging modalities.

6.3 Reflections on Image Acquisition

Reductions in acquisition time and injected activity have equal effects on image quality. Therefore, the results of acquisition time reduction can be applied in practice by reducing the injected activity instead. However, planar BS and bone SPECT-CT are most often performed in elderly cancer patients, for whom the reduction in acquisition time is typically more important than the reduction in radiation exposure. The relatively low radiation exposure of less than 10 mSv [24] from a whole-body bone SPECT-CT examination is clinically justified for elderly cancer patients, but laying still for almost an hour may be difficult for them. On the other hand, lower injected activities would also reduce staff radiation exposure.

The acquisition time per view, number of views, and the selection between step-and-shoot and continuous acquisition modes affect the time efficiency of image acquisition. In an efficient acquisition, the idle time required for detector and bed movements takes only a small portion of the total acquisition time. If the acquisition time per view is greatly reduced and the data are acquired in step-and-shoot mode with a large number of views, the idle time can take over half of the total acquisition time. Therefore, limiting the number of views might be even more important than limiting the acquisition time per view. This is further supported by the introduction of SPECT acquisition with as few as six views (12 projections), which, however, has not yet been validated for bone SPECT [208, 209]. Finally, continuous acquisition mode is the most time-efficient option, although it still requires careful balancing between acquisition time per view and number of views.

Another way to reduce the acquisition time even further would be to use two FOVs instead of three [127]. Two FOVs could cover the area from the base of the skull to proximal femurs, while three FOVs extend from the top of the skull to middle femurs. The excluded anatomical areas would unlikely contain solitary findings, as bone metastases are usually widespread when these areas are affected. The first areas where bone metastases typically occur are the spine, rib cage, and pelvis [210].

Energy-window narrowing decreased CNR without any apparent benefits. This may be explained by a limitation in SPECT acquisition software (NM Operator Console, version 1.003.611.0, GE Healthcare, Haifa, Israel) that does not allow changing of the detector uniformity correction matrix when energy window is changed. Ideally, different uniformity correction matrices would have been used with different energy windows [211]. Furthermore, the reconstruction software included a rather sophisticated scatter correction based on the CT attenuation map and Monte Carlo simulation, which may have diminished the effect of energy window narrowing. However, the difference in scatter correction performance between energy window

narrowing and simulation-based scatter correction remains unclear.

Nonetheless, with the CZT system, the use of a 15% energy window width is reasonable, especially when the acquisition time of bone SPECT is reduced. Energy window narrowing increases noise by reducing the number of accepted gamma rays, which results from the partial coverage of the measured photopeak. Assuming the CZT system has a Gaussian energy resolution with 6% FWHM at 140 keV, the energy windows centred at 140 keV with widths of 15, 10, 8, 6, and 4% would cover 99.6, 95, 88, 76, and 57% of the photopeak, respectively. The 15% energy window covers the photopeak almost completely.

Although the effects of acquisition time reduction were studied using only a digital CZT SPECT-CT system, the results can be generalized to analogic SPECT-CT systems by considering the differences in system sensitivity and spatial resolution. The acquisition time can be normalized with respect to the sensitivity difference between the SPECT-CT systems if they have similar spatial resolution.

6.4 Reflections on Image Processing

Although image processing was not thoroughly optimized in this thesis, it plays a critical role in the image quality and quantitative accuracy of bone SPECT. Currently, reconstructions are most often performed using iterative algorithms, which include corrections for photon attenuation, scatter, and collimator response. The trade-off between contrast and noise is controlled by iterations and filtering. More advanced reconstruction algorithms using CT for anatomical a priori information have been recently introduced [176, 183], but their accessibility was limited during the work of this thesis.

According to the quantitative and qualitative analyses of Study I, a noise level of approximately 0.10 was associated with clinically accepted image quality. This noise level was also used as the target when selecting filters for the 32- and 26-min images used in the diagnostic performance analysis. Otherwise in Study I, the reconstruction parameters were similar to those suggested to be optimal by Alqahtani et al. [87]. The 16-min images were processed differently to mimic the processing method used in a previous study by Gregoire et al. [25]. The short acquisition time combined with unoptimized image processing resulted in the highest number of equivocal lesions but had little effect on the patient- and region-level diagnostic performance.

In Study II, the typical image processing used for SPECT in this thesis was applied in the production of RBS images. This produced RBS images that were more detailed than the acquired BS images and had more numerous and intense focal uptakes. The RBS images also had clearly higher CNR than BS images, which was caused by the high contrast between bone and soft tissue and the smooth appearance of normal bone tissue. However, the increase in detail turned out rather counterproductive, as the RBS images contained many equivocal findings not reported from BS

images (Table 9).

In retrospect, it might have been suitable to use a less complex SPECT reconstruction for RBS images, i.e., lowering resolution by using fewer iterations and omitting corrections for scatter and collimator response. This could have caused RBS images to appear more like the acquired BS images. However, this would have also lowered the sensitivity of RBS closer to that of BS. Nonetheless, less complex processing should be considered in clinical practice if a follow-up RBS is compared with a previous BS.

In Study III, a higher number of iterations was used to compensate for the spatial resolution difference between SPECT and PET. A higher number of iterations increases the quantitation accuracy, but it also increases noise. Fortunately, algorithms incorporating relative difference priors are being incorporated into SPECT [176]. They allow the reconstruction of images with both low noise and accurate quantitation. Furthermore, the recently introduced algorithms using CT for anatomical a priori information increase the spatial resolution of bone SPECT but require acquisition using a 256×256 matrix [176, 183]. In Study I, the 256×256 matrix resulted in no apparent benefits for image quality, perhaps due to the use of the conventional reconstruction algorithm.

6.5 Topics for Further Research

Recently, CZT SPECT-CT systems with completely redesigned 3D acquisition geometry have been introduced [112, 212]. These systems have typically 12 detector heads positioned into a ring-shaped configuration. The acquisition protocols should be carefully optimized to make the most of these systems.

On the processing side, novel reconstruction algorithms should be optimized, especially for fast bone SPECT-CT. Furthermore, artificial intelligence has garnered attention in many fields, and nuclear medicine is no exception [213, 214]. Currently, the promising applications of artificial intelligence include image de-noising [215, 216] and automated image analysis [217, 218].

Finally, acquisition and reconstruction protocols should be standardized in such a way that quantitative results can be reliably compared between different hospitals and SPECT-CT systems. This requires more research on their quantitation accuracy and performance. For PET-CT, differences in absolute quantitation between various systems have been extensively characterized, leading to standardization through an accreditation program [219].

7 Conclusions

- I Whole-body bone SPECT-CT can be acquired using a general-purpose CZT system in less than 20 min without loss of diagnostic performance in metastasis staging of high-risk prostate cancer patients.
- II Whole-body bone SPECT-CT can be reprojected into more familiar anterior and posterior planar images with excellent sensitivity for bone metastases, making additional acquisition of planar BS unnecessary.
- III The SUVs of bone SPECT-CT and ^{18}F -NaF PET-CT correlate strongly and SUVRs are very similar, demonstrating that SPECT SUVs are feasible for uptake measurements in bone metastases of breast and prostate cancer.

Acknowledgements

The research for this thesis was carried out in the Department of Nuclear Medicine at the Turku University Hospital under the guidance of Adjunct Professors Tommi Nojonen and Marko Seppänen. I thank Tommi for introducing me to the field of nuclear medicine, for showing me the way in image processing and analysis, and most importantly, for teaching me to write by thoroughly reviewing all the manuscripts I drafted. I thank Marko for his clinical knowledge, insights on turning the research into practical results, and constant encouragement.

I thank Adjunct Professor Tiina Laitinen and Professor John Dickson for reviewing my thesis. Your feedback improved the quality of my thesis considerably. I am grateful to Adjunct Professor Outi Sipilä for having accepted to act as my opponent. I look forward to our discussion.

I appreciate the efforts of nuclear medicine specialists Kirsi Timonen, Simona Malaspina, Sorjo Mätzke, Pentti Rautio, Juho Raiko, Jukka Kemppainen, and radiologist Sami Kajander in image interpretation. Urologists Mikael Anttinen, Otto Ettala, Peter Boström, oncologist Anna Kuisma, and radiologist Ivan Jambor are acknowledged for sharing their rich patient data sets. I am also grateful to all the radiographers and laboratory technicians who acquired the patient data. Eliisa Löytyniemi is acknowledged for statistical support, and Antti Sohlberg for elaborating the principles behind the reconstruction algorithms used in the studies.

I thank chief physicist Mika Teräs for arranging me the physicist work complementing my thesis work. The thesis work was funded by the Emil Aaltonen Foundation, Turku University Hospital, University of Turku, Finnish Cultural Foundation, and Radiological Society of Finland. I thank all the physicists, radiographers, laboratory technologists, secretaries, ward domestics, and physicians I have worked with for providing the friendly working environments. Finally, I am grateful to my mother, father, sister, brother, wife and daughter for their support and affection, I love you all.

The 1st of August, 2024
Samuli Arvola

References

- [1] Gerstberger S, Jiang Q, Ganesh K. Metastasis. *Cell*. 2023;186:1564–1579.
- [2] Steeg PS. Tumor metastasis: mechanistic insights and clinical challenges. *Nat Med*. 2006;12:895–904.
- [3] Hamaoka T, Madewell JE, Podoloff DA, Hortobagyi GN, Ueno NT. Bone imaging in metastatic breast cancer. *J Clin Oncol*. 2004;22:2942–2953.
- [4] Mundy GR. Mechanisms of bone metastasis. *Cancer*. 1997;80:1546–1556.
- [5] Coleman RE, Croucher PI, Padhani AR, Clézardin P, Chow E, Fallon M, et al. Bone metastases. *Nat Rev Dis Primers*. 2020;6:83.
- [6] Cecchini MG, Wetterwald A, Pluijm Gvd, Thalmann GN. Molecular and biological mechanisms of bone metastasis. *EAU Update Ser*. 2005;3:214–226.
- [7] Ghanem N, Uhl M, Brink I, Schäfer O, Kelly T, Moser E, et al. Diagnostic value of MRI in comparison to scintigraphy, PET, MS-CT and PET/CT for the detection of metastases of bone. *Eur J Radiol*. 2005;55:41–55.
- [8] Histed SN, Lindenberg ML, Mena E, Turkbey B, Choyke PL, Kurdziel KA. Review of functional/anatomical imaging in oncology. *Nucl Med Commun*. 2012;33:349–361.
- [9] Orcajo-Rincon J, Muñoz-Langa J, Sepúlveda-Sánchez JM, Fernández-Pérez GC, Martínez M, Noriega-Álvarez E, et al. Review of imaging techniques for evaluating morphological and functional responses to the treatment of bone metastases in prostate and breast cancer. *Clin Transl Oncol*. 2022;24:1290–1310.
- [10] Israel O, Pellet O, Blassoni L, De Palma D, Estrada-Lobato E, Gnanasegaran G, et al. Two decades of SPECT/CT – the coming of age of a technology: an updated review of literature evidence. *Eur J Nucl Med Mol Imaging*. 2019;46:1990–2012.
- [11] Ell PJ, Dash J, Raymond J. Bone scanning: a review of purpose and method. *Skeletal Radiol*. 1976;1:33–45.
- [12] Love C, Din AS, Tomas MB, Kalappambath TP, Palestro CJ. Radionuclide bone imaging: an illustrative review. *Radiographics*. 2003;23:341–358.
- [13] Müller V, Steinhagen J, De Wit M, Bohuslavizki KH. Bone scintigraphy in clinical routine. *Radiol Oncol*. 2001;35:21–30.
- [14] Holder LE. Clinical radionuclide bone imaging. *Radiology*. 1990;176:607–614.
- [15] O'Connor MK, Brown ML, Hung JC, Hayostek RJ. The art of bone scintigraphy—technical aspects. *J Nucl Med*. 1991;32:2332–2341.
- [16] Rybak LD, Rosenthal DI. Radiological imaging for the diagnosis of bone metastases. *Q J Nucl Med*. 2001;45:53–64.
- [17] Savelli G, Maffioli L, Maccauro M, De Deckere E, Bombardieri E. Bone scintigraphy and the added value of SPECT (single photon emission tomography) in detecting skeletal lesions. *Q J Nucl Med*. 2001;45:27–37.
- [18] Utsunomiya D, Shiraishi S, Imuta M, Tomiguchi S, Kawanaka K, Morishita S, et al. Added value of SPECT/CT fusion in assessing suspected bone metastasis: comparison with scintigraphy alone and nonfused scintigraphy and CT. *Radiology*. 2006;238:264–271.
- [19] Jambor I, Kuisma A, Ramadan S, Huovinen R, Sandell M, Kajander S, et al. Prospective evaluation of planar bone scintigraphy, SPECT, SPECT/CT, 18F-NaF PET/CT and whole body 1.5T

- MRI, including DWI, for the detection of bone metastases in high risk breast and prostate cancer patients: SKELETA clinical trial. *Acta Oncol.* 2016;55:59–67.
- [20] Anttinen M, Ettala O, Malaspina S, Jambor I, Sandell M, Kajander S, et al. A prospective comparison of 18F-prostate-specific membrane antigen-1007 positron emission tomography computed tomography, whole-body 1.5 T magnetic resonance imaging with diffusion-weighted imaging, and single-photon emission computed tomography/computed tomography with traditional imaging in primary distant metastasis staging of prostate cancer (PROSTAGE). *Eur Urol Oncol.* 2020;4:635–644.
- [21] Mohseninia N, Zamani-Siahkali N, Harsini S, Divband G, Pirich C, Beheshti M. Bone metastasis in prostate cancer: bone scan versus PET imaging. *Semin Nucl Med.* 2024;54:97–118.
- [22] Ritt P, Sanders J, Kuwert T. SPECT/CT technology. *Clin Transl Imaging.* 2014;2:445–457.
- [23] Abikhzer G, Gourevich K, Kagna O, Israel O, Frenkel A, Keidar Z. Whole-body bone SPECT in breast cancer patients: the future bone scan protocol? *Nucl Med Comm.* 2016;37:247–253.
- [24] Van den Wyngaert T, Strobel K, Kampen WU, Kuwert T, van der Bruggen W, Mohan HK, et al. The EANM practice guidelines for bone scintigraphy. *Eur J Nucl Med Mol Imaging.* 2016;43:1723–1738.
- [25] Gregoire B, Pina-Jomir G, Bani-Sadr A, Moreau-Tribby C, Janier M, Scheiber C. Four-minute bone SPECT using large-field cadmium-zinc-telluride camera. *Clin Nucl Med.* 2018;43:389–395.
- [26] Bandi P, Zsoter N, Wirth A, Luetzen U, Derlin T, Papp L. New workflows and algorithms of bone scintigraphy based on SPECT-CT. *Annu Int Conf IEEE Eng Med Biol Soc.* 2012;2012:5971–5974.
- [27] Löfgren J, Mortensen J, Rasmussen SH, Madsen C, Loft A, Hansen AE, et al. A prospective study comparing 99mTc-hydroxyethylene-diphosphonate planar bone scintigraphy and whole-body SPECT/CT with 18F-fluoride PET/CT and 18F-fluoride PET/MRI for diagnosing bone metastases. *J Nucl Med.* 2017;58:1778–1785.
- [28] Meikle SR, Sossi V, Roncali E, Cherry SR, Banati R, Mankoff D, et al. Quantitative PET in the 2020s: a roadmap. *Phys Med Biol.* 2021;66:06RM01.
- [29] Goda HH, AbdAllah AEH, Ahmed EA, Megally HI, Khalaf MI, Taha AM, et al. Whole body diffusion-weighted MRI in detection of metastasis and lymphoma: a prospective longitudinal clinical study. *Egypt J Radiol Nucl Med.* 2020;51:141.
- [30] Jacobs MA, Macura KJ, Zaheer A, Antonarakis ES, Stearns V, Wolff AC, et al. Multiparametric whole-body MRI with diffusion-weighted imaging and ADC mapping for the identification of visceral and osseous metastases from solid tumors. *Acad Radiol.* 2018;25:1405–1414.
- [31] Koh DM, Blackledge M, Padhani AR, Takahara T, Kwee TC, Leach MO, et al. Whole-body diffusion-weighted MRI: tips, tricks, and pitfalls. *Am J Roentgenol.* 2012;199:252–262.
- [32] Bailey DL, Willowson KP. An evidence-based review of quantitative SPECT imaging and potential clinical applications. *J Nucl Med.* 2013;54:83–89.
- [33] Cachovan M, Vija AH, Hornegger J, Kuwert T. Quantification of 99mTc-DPD concentration in the lumbar spine with SPECT/CT. *EJNMMI Res.* 2013;3:1–8.
- [34] Sipilä O, Liukkonen J, Halme HL, Tolvanen T, Sohlberg A, Hakulinen M, et al. Variability in PET image quality and quantification measured with a permanently filled 68Ge-phantom: a multi-center study. *EJNMMI Phys.* 2023;10:38.
- [35] Messa C, Goodman WG, Hoh CK, Choi Y, Nissenson AR, Salusky IB, et al. Bone metabolic activity measured with positron emission tomography and 18F-fluoride ion in renal osteodystrophy: correlation with bone histomorphometry. *J Clin Endocrinol Metab.* 1993;77:949–955.
- [36] Piert M, Zittel TT, Becker GA, Jahn M, Stahlschmidt A, Maier G, et al. Assessment of porcine bone metabolism by dynamic 18F-fluoride PET: correlation with bone histomorphometry. *J Nucl Med.* 2001;42:1091–1100.
- [37] Lin C, Bradshaw T, Perk T, Harmon S, Eickhoff J, Jallow N, et al. Repeatability of quantitative 18F-NaF PET: a multicenter study. *J Nucl Med.* 2016;57:1872–1879.

- [38] Wassberg C, Lubberink M, Sörensen J, Johansson S. Repeatability of quantitative parameters of 18F-fluoride PET/CT and biochemical tumour and specific bone remodelling markers in prostate cancer bone metastases. *EJNMMI Res.* 2017;7:42–49.
- [39] Harper PV, Lathrop KA, Jiminez F, Fink R, Gottschalk A. Technetium 99m as a scanning agent. *Radiology.* 1965;85:101–109.
- [40] Atkins HL, Thomas SR, Buddemeyer U, Chervu LR. MIRDOSE report No. 14: radiation absorbed dose from technetium-99m-labeled red blood cells. *J Nucl Med.* 1990;31:378–380.
- [41] Bartel TB, Kuruva M, Gnanasegaran G, Cohen EJ, Weissman AF, Yarbrough TL. SNMMI procedure standard for bone scintigraphy 4.0. *J Nucl Med Technol.* 2018;46:398–404.
- [42] Roach PJ, Schembri GP, Ho Shon IA, Bailey EA, Bailey DL. SPECT/CT imaging using a spiral CT scanner for anatomical localization: Impact on diagnostic accuracy and reporter confidence in clinical practice. *Nucl Med Commun.* 2006;27:977–987.
- [43] Ritt P. Recent developments in SPECT/CT. *Semin Nucl Med.* 2022;52:276–285.
- [44] Van Audenhaege K, Van Holen R, Vandenberghe S, Vanhove C, Metzler SD, Moore SC. Review of SPECT collimator selection, optimization, and fabrication for clinical and preclinical imaging. *Med Phys.* 2015;42:4796–4813.
- [45] Rahmim A, Zaidi H. PET versus SPECT: strengths, limitations and challenges. *Nucl Med Commun.* 2008;29:193–207.
- [46] Peters SMB, van der Werf NR, Segbers M, van Velden FHP, Wierts R, Blokland K, et al. Towards standardization of absolute SPECT/CT quantification: a multi-center and multi-vendor phantom study. *EJNMMI Phys.* 2019;6:29.
- [47] King M, Farncombe T. An overview of attenuation and scatter correction of planar and SPECT data for dosimetry studies. *Cancer Biother Radiopharm.* 2003;18:181–190.
- [48] Ljungberg M, Pretorius PH. SPECT/CT: an update on technological developments and clinical applications. *Br J Radiol.* 2018;91:20160402.
- [49] Ardenfors O, Svanholm U, Jacobsson H, Sandqvist P, Grybäck P, Jonsson C. Reduced acquisition times in whole body bone scintigraphy using a noise-reducing Pixon®-algorithm—a qualitative evaluation study. *EJNMMI Res.* 2015;5:48.
- [50] Tsui BM, Beck RN, Doi K, Metz CE. Analysis of recorded image noise in nuclear medicine. *Phys Med Biol.* 1981;26:883–902.
- [51] Naddaf SY, Collier BD, Elgazzar AH, Khalil MM. Technical errors in planar bone scanning. *J Nucl Med Technol.* 2004;32:148–153.
- [52] Groch MW, Erwin WD. SPECT in the year 2000: basic principles. *J Nucl Med Technol.* 2000;28:233–244.
- [53] Seibert JA, Boone JM. X-Ray imaging physics for nuclear medicine technologists. Part 2: X-Ray interactions and image formation. *J Nucl Med Technol.* 2005;33:3–18.
- [54] Machado JMF, Doshi S, Smith R, Evans M, Graham RNJ, Redman S, et al. The effect of an asymmetric energy window on bone scintigraphy image quality. *J Nucl Med Technol.* 2020;48:46–50.
- [55] Jaszczak RJ, Coleman RE, Lim CB. SPECT: single photon emission computed tomography. *IEEE Trans Nucl Sci.* 1980;27:1137–1153.
- [56] Hutton BF. The origins of SPECT and SPECT/CT. *Eur J Nucl Med Mol Imaging.* 2014;41:3–16.
- [57] Kuwert T. Skeletal SPECT/CT: a review. *Clin Transl Imaging.* 2014;2:505–517.
- [58] Alqahtani M, Willowson K, Fulton R, Constable C, Kench P. Transition to fast whole-body SPECT/CT bone imaging: an assessment of image quality. *Diagnostics.* 2022;12:2938.
- [59] Bruyant PP. Analytic and iterative reconstruction algorithms in SPECT. *J Nucl Med.* 2002;43:1343–1358.
- [60] Hutton BF. Recent advances in iterative reconstruction for clinical SPECT/PET and CT. *Acta Oncol.* 2011;50:851–858.
- [61] Vandenberghe S, D’Asseler Y, Van de Walle R, Kauppinen T, Koole M, Bouwens L, et al. Iterative reconstruction algorithms in nuclear medicine. *Comput Med Imaging Graph.* 2001;25:105–111.

- [62] Hudson HM, Larkin RS. Accelerated image reconstruction using ordered subsets of projection data. *IEEE Trans Med Imaging*. 1994;13:601–609.
- [63] Shepp LA, Vardi Y. Maximum likelihood reconstruction for emission tomography. *IEEE Trans Med Imaging*. 1982;1:113–122.
- [64] Lange K, Carson R. EM reconstruction algorithms for emission and transmission tomography. *J Comput Assist Tomogr*. 1984;8:306–316.
- [65] Cleveland BT. The analysis of radioactive decay with a small number of counts by the method of maximum likelihood. *Nucl Instrum Methods Phys Res*. 1983;214:451–458.
- [66] Seo Y, Wong KH, Sun M, Franc BL, Hawkins RA, Hasegawa BH. Correction of photon attenuation and collimator response for a body-contouring SPECT/CT imaging system. *J Nucl Med*. 2005;46:868–877.
- [67] Patton JA, Turkington TG. SPECT/CT physical principles and attenuation correction. *J Nucl Med Technol*. 2008;36:1–10.
- [68] Zaidi H, Hasegawa B. Determination of the attenuation map in emission tomography. *J Nucl Med*. 2003;44:291–315.
- [69] LaCroix KJ, Tsui BMW, Hasegawa BH, Brown JK. Investigation of the use of X-ray CT images for attenuation compensation in SPECT. *IEEE Trans on Nucl Sci*. 1994;41:2793–2799.
- [70] Blankespoor SC, Xu X, Kaiki K, Brown JK, Tang HR, Cann CE, et al. Attenuation correction of SPECT using X-ray CT on an emission-transmission CT system: myocardial perfusion assessment. *IEEE Trans Nucl Sci*. 1996;43:2263–2274.
- [71] Hutton BF, Buvat I, Beekman FJ. Review and current status of SPECT scatter correction. *Phys Med Biol*. 2011;56:R85–R112.
- [72] Ljungberg M, Strand SE. Scatter and attenuation correction in SPECT using density maps and Monte Carlo simulated scatter functions. *J Nucl Med*. 1990;31:1560–1567.
- [73] Jaszczak RJ, Greer KL, Carey E, Floyd J, Harris CC, Coleman RE. Improved SPECT quantification using compensation for scattered photons. *J Nucl Med*. 1984;25:893–900.
- [74] Zaidi H, Koral KF. Scatter modelling and compensation in emission tomography. *Eur J Nucl Med Mol Imaging*. 2004;31:761–782.
- [75] Carey E, Floyd J, Jaszczak RJ, Greer KL, Coleman RE. Inverse Monte Carlo as a unified reconstruction algorithm for ECT. *J Nucl Med*. 1986;27:1577–1585.
- [76] Jong HWAMd, Slijpen ETP, Beekman FJ. Acceleration of Monte Carlo SPECT simulation using convolution-based forced detection. *IEEE Trans Nucl Sci*. 2001;48:58–64.
- [77] Sohlberg A, Watabe H, Iida H. Acceleration of Monte Carlo-based scatter compensation for cardiac SPECT. *Phys Med Biol*. 2008;53:N277–N285.
- [78] Beekman FJ, de Jong HWAM, van Geloven S. Efficient fully 3-D iterative SPECT reconstruction with Monte Carlo-based scatter compensation. *IEEE Trans Med Imaging*. 2002;21:867–877.
- [79] Kamphuis C, Beekman FJ, van Rijk PP, Viergever MA. Dual matrix ordered subsets reconstruction for accelerated 3D scatter compensation in single-photon emission tomography. *Eur J Nucl Med*. 1998;25:8–18.
- [80] Beekman FJ, de Jong HWAM, Slijpen ETP. Efficient SPECT scatter calculation in non-uniform media using correlated Monte Carlo simulation. *Phys Med Biol*. 1999;44:N183–N192.
- [81] Moore SC, Kouris K, Cullum I. Collimator design for single photon emission tomography. *Eur J Nucl Med*. 1992;19:138–150.
- [82] Chun SY, Fessler JA, Dewaraja YK. Correction for collimator-detector response in SPECT using point spread function template. *IEEE Trans Med Imaging*. 2013;32:295–305.
- [83] Formiconi AR, Pupi A, Passeri A. Compensation of spatial system response in SPECT with conjugate gradient reconstruction technique. *Phys Med Biol*. 1989;34:69.
- [84] Nuyts J, Beque D, Dupont P, Mortelmans L. A concave prior penalizing relative differences for maximum-a-posteriori reconstruction in emission tomography. *IEEE Trans Nucl Sci*. 2002;49:56–60.
- [85] Lyra M, Ploussi A. Filtering in SPECT image reconstruction. *Int J Biomed Imaging*. 2011;2011:693795.

- [86] Gilland DR, Tsui BMW, McCartney WH, Perry JR, Berg J. Determination of the optimum filter function for SPECT imaging. *J Nucl Med.* 1988;29:643–650.
- [87] Alqahtani MM, Willowson KP, Constable C, Fulton R, Kench PL. Optimization of ^{99m}Tc whole-body SPECT/CT image quality: a phantom study. *J Appl Clin Med Phys.* 2022;23:e13528.
- [88] Seret A. The number of subsets required for OSEM reconstruction in nuclear cardiology. *Eur J Nucl Med Mol Imaging.* 2006;33:231.
- [89] Mariani G, Bruselli L, Kuwert T, Kim EE, Flotats A, Israel O, et al. A review on the clinical uses of SPECT/CT. *Eur J Nucl Med Mol Imaging.* 2010;37:1959–1985.
- [90] Townsend DW. Dual-modality imaging: combining anatomy and function. *J Nucl Med.* 2008;49:938–955.
- [91] Beyer T, Veit-Haibach P. State-of-the-art SPECT/CT: technology, methodology and applications—defining a new role for an undervalued multimodality imaging technique. *Eur J Nucl Med Mol Imaging.* 2014;41:S1–S2.
- [92] Kalender WA. X-ray computed tomography. *Phys Med Biol.* 2006;51:R29.
- [93] Klingenberg-Regn K, Schaller S, Flohr T, Ohnesorge B, Kopp AF, Baum U. Subsecond multi-slice computed tomography: basics and applications. *Eur J Radiol.* 1999;31:110–124.
- [94] Flohr T. CT systems. *Curr Radiol Rep.* 2013;1:52–63.
- [95] Zhang R, Thibault JB, Bouman CA, Sauer KD, Hsieh J. Model-based iterative reconstruction for dual-energy X-ray CT using a joint quadratic likelihood model. *IEEE Trans Med Imaging.* 2014;33:117–134.
- [96] Kim JH, Nuyts J, Kyme A, Kuncic Z, Fulton R. A rigid motion correction method for helical computed tomography (CT). *Phys Med Biol.* 2015;60:2047.
- [97] Gottumukkala RV, Kalra MK, Tabari A, Otrajki A, Gee MS. Advanced CT techniques for decreasing radiation dose, reducing sedation requirements, and optimizing image quality in children. *Radiographics.* 2019;39:709–726.
- [98] Willemink MJ, de Jong PA, Leiner T, de Heer LM, Nijelstein RAJ, Budde RPJ, et al. Iterative reconstruction techniques for computed tomography Part 1: technical principles. *Eur Radiol.* 2013;23:1623–1631.
- [99] Willemink MJ, Noël PB. The evolution of image reconstruction for CT—from filtered back projection to artificial intelligence. *Eur Radiol.* 2019;29:2185–2195.
- [100] Johns PM, Nino JC. Room temperature semiconductor detectors for nuclear security. *J Appl Phys.* 2019;126:040902.
- [101] Meikle SR, Kench P, Kassiou M, Banati RB. Small animal SPECT and its place in the matrix of molecular imaging technologies. *Phys Med Biol.* 2005;50:R45.
- [102] Madsen MT. Recent advances in SPECT imaging. *J Nucl Med.* 2007;48:661–673.
- [103] Anger HO. Scintillation Camera. *Rev Sci Instrum.* 1958;29:27–33.
- [104] Ito T, Matsusaka Y, Onoguchi M, Ichikawa H, Okuda K, Shibutani T, et al. Experimental evaluation of the GE NM/CT 870 CZT clinical SPECT system equipped with WEHR and MEHRS collimator. *J Appl Clin Med Phys.* 2021;22:165–177.
- [105] Salgado CM, Brandão LEB, Schirru R, Pereira CMNA, Conti CC. Validation of a NaI(Tl) detector’s model developed with MCNP-X code. *Prog Nucl Energy.* 2012;59:19–25.
- [106] Mueller B, O’Connor MK, Blevis I, Rhodes DJ, Smith R, Collins DA, et al. Evaluation of a small cadmium zinc telluride detector for scintimammography. *J Nucl Med.* 2003;44:602–609.
- [107] Zheng X, Cheng Z, Deen MJ, Peng H. Improving the spatial resolution in CZT detectors using charge sharing effect and transient signal analysis: Simulation study. *Nucl Instrum Methods Phys Res A.* 2016;808:60–70.
- [108] Peterson TE, Furenlid LR. SPECT detectors: the Anger Camera and beyond. *Phys Med Biol.* 2011;56:R145.
- [109] Hutton BF, Erlandsson K, Thielemans K. Advances in clinical molecular imaging instrumentation. *Clin Transl Imaging.* 2018;6:31–45.

- [110] Noponen T, Tsukerman L, Kiiliäinen H, Seppänen M, Knuuti J. Comparison of performances of analogical and digital SPECT/CT imaging systems. *Eur J Nucl Med Mol Imaging*. 2018;45:S17.
- [111] Gambhir SS, Berman DS, Ziffer J, Nagler M, Sandler M, Patton J, et al. A novel high-sensitivity rapid-acquisition single-photon cardiac imaging camera. *J Nucl Med*. 2009;50:635–643.
- [112] Goshen E, Beilin L, Stern E, Kenig T, Goldkorn R, Ben-Haim S. Feasibility study of a novel general purpose CZT-based digital SPECT camera: initial clinical results. *EJNMMI Phys*. 2018;5:6.
- [113] Nudi F, Iskandrian AE, Schillaci O, Peruzzi M, Frati G, Biondi-Zoccai G. Diagnostic accuracy of myocardial perfusion imaging with CZT technology: systemic review and meta-analysis of comparison with invasive coronary angiography. *JACC Cardiovasc Imaging*. 2017;10:787–794.
- [114] Cantoni V, Green R, Acampa W, Zampella E, Assante R, Nappi C, et al. Diagnostic performance of myocardial perfusion imaging with conventional and CZT single-photon emission computed tomography in detecting coronary artery disease: A meta-analysis. *J Nucl Cardiol*. 2021;28:698–715.
- [115] Panjer M, Dobrolinska M, Wagenaar NRL, Slart RHJA. Diagnostic accuracy of dynamic CZT-SPECT in coronary artery disease. A systematic review and meta-analysis. *J Nucl Cardiol*. 2022;29:1686–1697.
- [116] Desmots C, Bouthiba MA, Enilorac B, Nganoa C, Agostini D, Aide N. Evaluation of a new multipurpose whole-body CzT-based camera: comparison with a dual-head Anger camera and first clinical images. *EJNMMI Phys*. 2020;7:18.
- [117] Yamane T, Kondo A, Takahashi M, Miyazaki Y, Ehara T, Koga K, et al. Ultrafast bone scintigraphy scan for detecting bone metastasis using a CZT whole-body gamma camera. *Eur J Nucl Med Mol Imaging*. 2019;46:1672–1677.
- [118] Bahloul A, Verger A, Blum A, Chawki MB, Perrin M, Melki S, et al. Bone scintigraphy of vertebral fractures with a whole-body CZT camera in a PET-like utilization. *Front Nucl Med*. 2021;1:740275.
- [119] Madsen MT. Computer acquisition of nuclear medicine images. *J Nucl Med Technol*. 1994;22:3–11.
- [120] Mavriopoulou E, Zampakis P, Smpiliri E, Spyridonidis T, Rapti E, Haberkorn U, et al. Whole body bone SPET/CT can successfully replace the conventional bone scan in breast cancer patients. A prospective study of 257 patients. *Hell J Nucl Med*. 2018;21:125–133.
- [121] Alqahtani MM, Fulton R, Constable C, Willowson KP, Kench PL. Diagnostic performance of whole-body SPECT/CT in bone metastasis detection using (99m)Tc-labelled diphosphate: a systematic review and meta-analysis. *Clin Radiol*. 2020;75:961.e11–961.e24.
- [122] Palmedo H, Marx C, Ebert A, Kreft B, Ko Y, Türler A, et al. Whole-body SPECT/CT for bone scintigraphy: diagnostic value and effect on patient management in oncological patients. *Eur J Nucl Med Mol Imaging*. 2014;41:59–67.
- [123] Rager O, Nkoulou R, Exquis N, Garibotto V, Tabouret-Viaud C, Zaidi H, et al. Whole-body SPECT/CT versus planar bone scan with targeted SPECT/CT for metastatic workup. *Biomed Res Int*. 2017;2017:7039406.
- [124] Even-Sapir E, Metser U, Mishani E, Lievshitz G, Lerman H, Leibovitch I. The detection of bone metastases in patients with high-risk prostate cancer: 99mTc-MDP Planar bone scintigraphy, single- and multi-field-of-view SPECT, 18F-fluoride PET, and 18F-fluoride PET/CT. *J Nucl Med*. 2006;47:287–297.
- [125] Fonager RF, Zacho HD, Langkilde NC, Fledelius J, Ejlersen JA, Haarmark C, et al. Diagnostic test accuracy study of 18F-sodium fluoride PET/CT, 99mTc-labelled diphosphonate SPECT/CT, and planar bone scintigraphy for diagnosis of bone metastases in newly diagnosed, high-risk prostate cancer. *Am J Nucl Med Mol Imaging*. 2017;7:218–227.
- [126] Guezennec C, Keromnes N, Robin P, Abgral R, Bourhis D, Querellou S, et al. Incremental diagnostic utility of systematic double-bed SPECT/CT for bone scintigraphy in initial staging of cancer patients. *Cancer Imaging*. 2017;17:16.

- [127] Fleury V, Ferrer L, Colombié M, Rusu D, Le Thiec M, Kraeber-Bodéré F, et al. Advantages of systematic trunk SPECT/CT to planar bone scan (PBS) in more than 300 patients with breast or prostate cancer. *Oncotarget*. 2018;9:31744–31752.
- [128] Jaszczak RJ, Whitehead FR, Lim CB, Coleman RE. Lesion detection with single-photon emission computed tomography (SPECT) compared with conventional imaging. *J Nucl Med*. 1982;23:97–102.
- [129] Langsteger W, Rezaee A, Pirich C, Beheshti M. ¹⁸F-NaF-PET/CT and ^{99m}Tc-MDP bone scintigraphy in the detection of bone metastases in prostate cancer. *Semin Nucl Med*. 2016;46:491–501.
- [130] Coleman RE. Clinical features of metastatic bone disease and risk of skeletal morbidity. *Clin Cancer Res*. 2006;12:6243s–6249s.
- [131] Simsek DH, Sanli Y, Kuyumcu S, Engin MN, Buyukkaya F, Demirci E. Clinical impact of lower-limb imaging in ⁶⁸Ga-PSMA PET/CT for patients with prostate cancer. *J Nucl Med Technol*. 2019;47:233–237.
- [132] Melki S, Chawki MB, Marie P, Imbert L, Verger A. Augmented planar bone scintigraphy obtained from a whole-body SPECT recording of less than 20 min with a high-sensitivity 360° CZT camera. *Eur J Nucl Med Mol Imaging*. 2020;47:1329–1331.
- [133] Andelius IC, Minarik D, Persson E, Mosén H, Valind K, Trägårdh E, et al. First clinical experience of a ring-configured cadmium zinc telluride camera: a comparative study versus conventional gamma camera systems. *Clin Physiol Funct Imaging*. 2024;44:79–88.
- [134] Le Roux PY, Abgral R, Jaffrelot M, Delluc A, Gut-Gobert C, Querellou S, et al. Diagnosis of pulmonary embolism: planar images generated from V/Q SPECT are not a reliable substitute for traditional planar V/Q scan. *Nucl Med Commun*. 2012;33:695–700.
- [135] Bailey DL, Schembri GP, Harris BE, Bailey EA, Cooper RA, Roach PJ. Generation of planar images from lung ventilation/perfusion SPECT. *Ann Nucl Med*. 2008;22:437–445.
- [136] Harris B, Bailey DL, Roach PJ, Schembri GP, HoShon I, Chicco P, et al. A clinical comparison between traditional planar V/Q images and planar images generated from SPECT V/Q scintigraphy. *Nucl Med Commun*. 2008;29:323–330.
- [137] Kyrtatos PG, Navalkisoor S, Burniston M, Wagner T. Planar images reprojected from SPECT V/Q data perform similarly to traditional planar V/Q scans in the diagnosis of pulmonary embolism. *Nucl Med Comm*. 2013;34:445–450.
- [138] Wells RG, Marvin B, Kovalski G, Ruddy TD. Planar radionuclide angiography with a dedicated cardiac SPECT camera. *J Nucl Cardiol*. 2013;20:358–366.
- [139] O'Doherty J, Rojas Fisher B, Price JM, Wechalekar K. Assessment of an intermediate re-projection technique transitioning from planar to SPECT radionuclide ventriculography. *J Nucl Cardiol*. 2014;21:944–953.
- [140] Willowson K, Bailey DL, Baldock C. Quantitative SPECT reconstruction using CT-derived corrections. *Phys Med Biol*. 2008;53:3099–3112.
- [141] Shcherbinin S, Celler A, Belhocine T, Vanderwerf R, Driedger A. Accuracy of quantitative reconstructions in SPECT/CT imaging. *Phys Med Biol*. 2008;53:4595.
- [142] Zeintl J, Vija AH, Yahil A, Hornegger J, Kuwert T. Quantitative accuracy of clinical ^{99m}Tc SPECT/CT using ordered-subset expectation maximization with 3-dimensional resolution recovery, attenuation, and scatter correction. *J Nucl Med*. 2010;51:921–928.
- [143] Bailey DL, Willowson KP. Quantitative SPECT/CT: SPECT joins PET as a quantitative imaging modality. *Eur J Nucl Med Mol Imaging*. 2014;41:S17–S25.
- [144] Dewaraja YK, Frey EC, Sgouros G, Brill AB, Roberson P, Zanzonico PB, et al. MIRD pamphlet No. 23: quantitative SPECT for patient-specific 3-dimensional dosimetry in internal radionuclide therapy. *J Nucl Med*. 2012;53:1310–1325.
- [145] Römer W, Nömayr A, Uder M, Bautz W, Kuwert T. SPECT-guided CT for evaluating foci of increased bone metabolism classified as indeterminate on SPECT in cancer patients. *J Nucl Med*. 2006;47:1102–1106.

- [146] Beck M, Sanders JC, Ritt P, Reinfelder J, Kuwert T. Longitudinal analysis of bone metabolism using SPECT/CT and ^{99m}Tc-diphosphonopropanedicarboxylic acid: comparison of visual and quantitative analysis. *EJNMMI Res.* 2016;6:60–68.
- [147] Kaneta T, Ogawa M, Daisaki H, Nawata S, Yoshida K, Inoue T. SUV measurement of normal vertebrae using SPECT/CT with Tc-99m methylene diphosphonate. *Am J Nucl Med Mol Imaging.* 2016;6:262–268.
- [148] Ross JC, Vilić D, Sanderson T, Vöö S, Dickson J. Does quantification have a role to play in the future of bone SPECT? *Eur J Hybrid Imaging.* 2019;3:8.
- [149] Lockhart CM, MacDonald LR, Alessio AM, McDougald WA, Doot RK, Kinahan PE. Quantifying and reducing the effect of calibration error on variability of PET/CT standardized uptake value measurements. *J Nucl Med.* 2011;52:218–224.
- [150] Cheebsumon P, Velasquez LM, Hoekstra CJ, Hayes W, Kloet RW, Hoetjes NJ, et al. Measuring response to therapy using FDG PET: semi-quantitative and full kinetic analysis. *Eur J Nucl Med Mol Imaging.* 2011;38:832–842.
- [151] Front D, Israel O, Jerushalmi J, Frenkel A, Iosilevsky G, Feinsod M, et al. Quantitative bone scintigraphy using SPECT. *J Nucl Med.* 1989;30:240–245.
- [152] Israel O, Front D, Hardoff R, Ish-Shalom S, Jerushalmi J, Kolodny GM. In vivo SPECT quantitation of bone metabolism in hyperparathyroidism and thyrotoxicosis. *J Nucl Med.* 1991;32:1157–1161.
- [153] Israel O, Lubushitzky R, Frenkel A, Iosilevsky G, Bettman L, Gips S, et al. Bone turnover in cortical and trabecular bone in normal women and in women with osteoporosis. *J Nucl Med.* 1994;35:1155–1158.
- [154] Israel O, Gips S, Hardoff R, Rudoy J, Frajewicki V, Iosilevsky G, et al. Bone loss in patients with chronic renal disease: prediction with quantitative bone scintigraphy with SPECT. *Radiology.* 1995;196:643–646.
- [155] Yamane T, Fukushima K, Shirotake S, Nishimoto K, Okabe T, Oyama M, et al. Test–retest repeatability of quantitative bone SPECT/CT. *Ann Nucl Med.* 2021;35:338–346.
- [156] Tabotta F, Jreige M, Schaefer N, Becce F, Prior JO, Nicod Lalonde M. Quantitative bone SPECT/CT: high specificity for identification of prostate cancer bone metastases. *BMC Musculoskelet Disord.* 2019;20:619.
- [157] Kuji I, Yamane T, Seto A, Yasumizu Y, Shirotake S, Oyama M. Skeletal standardized uptake values obtained by quantitative SPECT/CT as an osteoblastic biomarker for the discrimination of active bone metastasis in prostate cancer. *Eur J Hybrid Imaging.* 2017;1:2–17.
- [158] Vija AH, Bartenstein PA, Froelich JW, Kuwert T, Macapinlac H, Daignault CP, et al. ROC study and SUV threshold using quantitative multi-modal SPECT for bone imaging. *Eur J Hybrid Imaging.* 2019;3:10.
- [159] Mohd Rohani MF, Mat Nawi N, Shamim SE, Wan Sohaimi WF, Wan Zainon WMN, Musarudin M, et al. Maximum standardized uptake value from quantitative bone single-photon emission computed tomography/computed tomography in differentiating metastatic and degenerative joint disease of the spine in prostate cancer patients. *Ann Nucl Med.* 2020;34:39–48.
- [160] Qi N, Meng Q, You Z, Chen H, Shou Y, Zhao J. Standardized uptake values of ^{99m}Tc-MDP in normal vertebrae assessed using quantitative SPECT/CT for differentiation diagnosis of benign and malignant bone lesions. *BMC Med Imaging.* 2021;21:39.
- [161] Gherghe M, Mutuleanu MD, Stanciu AE, Irimescu I, Lazar A, Bacinschi X, et al. Quantitative analysis of SPECT-CT data in metastatic breast cancer patients—the clinical significance. *Cancers.* 2022;14:273.
- [162] Lin L, Zheng R, Geng J, Wang X, Li M, Fan R, et al. Skeletal standardized uptake values obtained using quantitative SPECT/CT for the detection of bone metastases in patients with lung adenocarcinoma. *Front Med.* 2023;10:1119214.
- [163] Du F, Wumener X, Zhang Y, Liu M, Li T, Huang S, et al. The diagnostic value of quantitative bone SPECT/CT in solitary undetermined bone lesions. *Front Oncol.* 2023;13:1205379.

- [164] Kitajima K, Futani H, Fujiwara M, Minakawa G, Osugi Y, Tsuchitani T, et al. Usefulness of quantitative bone single photon emission computed tomography/computed tomography for evaluating response to neoadjuvant chemotherapy in a patient with periosteal osteosarcoma. *Cureus*. 2018;10:e3655.
- [165] Kitajima K, Tsuchitani T, Takahashi Y, Minami T, Yokoi T, Nakamura A, et al. Usefulness of quantitative bone single-photon emission computed tomography/computed tomography for evaluating the treatment response of bone metastasis in a lung cancer patient. *Case Rep Oncol*. 2021;14:391–396.
- [166] Komoto H, Kitajima K, Azuma N, Tamura M, Yokoyama H, Tsuchitani T, et al. Quantitative bone SPECT/CT for evaluating treatment response in patient with sternoclavicular arthritis. *Acta Radiol Open*. 2022;11:20584601221128409.
- [167] Gherghe M, Mutuleanu MD, Stanciu AE, Irimescu I, Lazar AM, Toma RV, et al. Quantitative assessment of treatment response in metastatic breast cancer patients by SPECT-CT bone imaging—getting closer to PET-CT. *Cancers*. 2023;15:696.
- [168] Oya T, Ichikawa Y, Nakamura S, Tomita Y, Sasaki T, Inoue T, et al. Quantitative assessment of ^{99m}Tc-methylene diphosphonate bone SPECT/CT for assessing bone metastatic burden and its prognostic value in patients with castration-resistant prostate cancers: initial results in a single-center retrospective study. *Ann Nucl Med*. 2023;37:360–370.
- [169] Braun M, Cachovan M, Kaul F, Caobelli F, Bäumer M, Hans Vija A, et al. Accuracy comparison of various quantitative [^{99m}Tc]Tc-DPD SPECT/CT reconstruction techniques in patients with symptomatic hip and knee joint prostheses. *EJNMMI Res*. 2021;11:60.
- [170] Kim J, Lee HH, Kang Y, Kim TK, Lee SW, So Y, et al. Maximum standardised uptake value of quantitative bone SPECT/CT in patients with medial compartment osteoarthritis of the knee. *Clin Radiol*. 2017;72:580–589.
- [171] Huang K, Feng Y, Liu D, Liang W, Li L. Quantification evaluation of ^{99m}Tc-MDP concentration in the lumbar spine with SPECT/CT: compare with bone mineral density. *Ann Nucl Med*. 2020;34:136–143.
- [172] Yamane T, Kuji I, Seto A, Matsunari I. Quantification of osteoblastic activity in epiphyseal growth plates by quantitative bone SPECT/CT. *Skeletal Radiol*. 2018;47:805–810.
- [173] Ritt P, Vija H, Hornegger J, Kuwert T. Absolute quantification in SPECT. *Eur J Nucl Med Mol Imaging*. 2011;38:S69–S77.
- [174] Rosenthal MS, Cullom J, Hawkins W, Moore SC, Tsui BMW, Yester M. Quantitative SPECT imaging: a review and recommendations by the Focus Committee of the Society of Nuclear Medicine Computer and Instrumentation Council. *J Nucl Med*. 1995;36:1489–1513.
- [175] Green PJ. Bayesian reconstructions from emission tomography data using a modified EM algorithm. *IEEE Trans Med Imaging*. 1990;9:84–93.
- [176] Kangasmaa TS, Constable C, Sohlberg AO. Quantitative bone SPECT/CT reconstruction utilizing anatomical information. *EJNMMI Phys*. 2021;2021:2.
- [177] Bowsher JE, Johnson VE, Turkington TG, Jaszczak RJ, Floyd CE, Coleman RE. Bayesian reconstruction and use of anatomical a priori information for emission tomography. *IEEE Trans Med Imaging*. 1996;15:673–686.
- [178] Vuohijoki HE, Constable CJ, Sohlberg AO. Anatomically guided reconstruction improves lesion quantitation and detectability in bone SPECT/CT. *Nucl Med Commun*. 2023;44:330–337.
- [179] Okuda K, Fujii S, Sakimoto S. Impact of novel incorporation of CT-based segment mapping into a conjugated gradient algorithm on bone SPECT imaging: fundamental characteristics of a context-specific reconstruction method. *Asia Ocean J Nucl Med Biol*. 2019;7:49–57.
- [180] Miyaji N, Miwa K, Tokiwa A, Ichikawa H, Terauchi T, Koizumi M, et al. Phantom and clinical evaluation of bone SPECT/CT image reconstruction with xSPECT algorithm. *EJNMMI Res*. 2020;10:71.
- [181] Lima TVM, Bhure U, Pérez Lago MdS, Thali Y, Matijasevic S, Roos J, et al. Impact of metal implants on xSPECT/CT Bone reconstruction: the “shining metal artefact”. *Eur J Hybrid Imaging*. 2020;4:18.

- [182] Delcroix O, Robin P, Gouillou M, Le Duc-Pennec A, Alavi Z, Le Roux PY, et al. A new SPECT/CT reconstruction algorithm: reliability and accuracy in clinical routine for non-oncologic bone diseases. *EJNMMI Res.* 2018;8:14.
- [183] Duncan I, Ingold N. The clinical value of xSPECT/CT Bone versus SPECT/CT. A prospective comparison of 200 scans. *Eur J Hybrid Imaging.* 2018;2:4.
- [184] Ichikawa H, Miyaji N, Onoguchi M, Shibutani T, Nagaki A, Kato T, et al. Feasibility of ultra-high-speed acquisition in xSPECT bone algorithm: a phantom study with advanced bone SPECT-specific phantom. *Ann Nucl Med.* 2022;36:183–190.
- [185] Kangasmaa T, Sohlberg A, Kuikka JT. Reduction of collimator correction artefacts with Bayesian reconstruction in Spect. *Int J Mol Imaging.* 2011;2011:630813.
- [186] Bexelius T, Sohlberg A. Implementation of GPU accelerated SPECT reconstruction with Monte Carlo-based scatter correction. *Ann Nucl Med.* 2018;32:337–347.
- [187] Turkington TG. Introduction to PET instrumentation. *J Nucl Med Technol.* 2001;29:4–11.
- [188] Goud NS, Joshi RK, Bharath RD, Kumar P. Fluorine-18: a radionuclide with diverse range of radiochemistry and synthesis strategies for target based PET diagnosis. *Eur J Med Chem.* 2020;187:111979.
- [189] Beheshti M, Mottaghy FM, Payche F, Behrendt FFF, Van den Wyngaert T, Fogelman I, et al. 18F-NaF PET/CT: EANM procedure guidelines for bone imaging. *Eur J Nucl Med Mol Imaging.* 2015;42:1767–1777.
- [190] Fendler WP, Eiber M, Beheshti M, Bomanji J, Calais J, Ceci F, et al. PSMA PET/CT: joint EANM procedure guideline/SNMMI procedure standard for prostate cancer imaging 2.0. *Eur J Nucl Med Mol Imaging.* 2023;50:1466–1486.
- [191] Karp JS, Surti S, Daube-Witherspoon ME, Muehllehner G. Benefit of time-of-flight in PET: experimental and clinical results. *J Nucl Med.* 2008;49:462–470.
- [192] Sheikhabaei S, Jones KM, Werner RA, Salas-Fragomeni RA, Marcus CV, Higuchi T, et al. 18F-NaF-PET/CT for the detection of bone metastasis in prostate cancer: a meta-analysis of diagnostic accuracy studies. *Ann Nucl Med.* 2019;33:351–361.
- [193] Smith-Bindman R, Lipson J, Marcus R, Kim KP, Mahesh M, Gould R, et al. Radiation dose associated with common computed tomography examinations and the associated lifetime attributable risk of cancer. *Arch Intern Med.* 2009;169:2078–2086.
- [194] Lusic H, Grinstaff MW. X-ray-computed tomography contrast agents. *Chem Rev.* 2013;113:1641–1666.
- [195] Lee YH, Kim S, Lim D, Suh JS, Song HT. Spectral parametric segmentation of contrast-enhanced dual-energy CT to detect bone metastasis: feasibility sensitivity study using whole-body bone scintigraphy. *Acta Radiol.* 2015;56:458–464.
- [196] Yang HL, Liu T, Wang XM, Xu Y, Deng SM. Diagnosis of bone metastases: a meta-analysis comparing 18FDG PET, CT, MRI and bone scintigraphy. *Eur Radiol.* 2011;21:2604–2617.
- [197] Pooley RA. Fundamental physics of MR imaging. *Radiographics.* 2005;25:1087–1099.
- [198] Gossuin Y, Hocq A, Gillis P, Quoc Lam V. Physics of magnetic resonance imaging: from spin to pixel. *J Phys D Appl Phys.* 2010;43:213001.
- [199] Pinker K, Ba-Ssalamah A, Wolfsberger S, Mlynarik V, Knosp E, Trattnig S. The value of high-field MRI (3T) in the assessment of sellar lesions. *Eur J Radiol.* 2005;54:327–334.
- [200] Stecco A, Trisoglio A, Soligo E, Berardo S, Sukhovei L, Carriero A. Whole-body MRI with diffusion-weighted imaging in bone metastases: a narrative review. *Diagnostics.* 2018;8:45.
- [201] Luypaert R, Boujraf S, Sourbron S, Osteaux M. Diffusion and perfusion MRI: basic physics. *Eur J Radiol.* 2001;38:19–27.
- [202] Koh DM, Collins DJ. Diffusion-weighted MRI in the body: applications and challenges in oncology. *Am J Roentgenol.* 2007;188:1622–1635.
- [203] Evangelista L, Bertoldo F, Boccardo F, Conti G, Menchi I, Mungai F, et al. Diagnostic imaging to detect and evaluate response to therapy in bone metastases from prostate cancer: current modalities and new horizons. *Eur J Nucl Med Mol Imaging.* 2016;43:1546–1562.

- [204] Kangasmaa TS, Constable C, Hippeläinen E, Sohlberg AO. Multicenter evaluation of single-photon emission computed tomography quantification with third-party reconstruction software. *Nucl Med Commun.* 2016;37:983–987.
- [205] Brenner AI, Koshy J, Morey J, Lin C, DiPoce J. The bone scan. *Semin Nucl Med.* 2012;42:11–26.
- [206] Yamane T, Takahashi M, Matsusaka Y, Fukushima K, Seto A, Kuji I, et al. Satisfied quantitative value can be acquired by short-time bone SPECT/CT using a whole-body cadmium–zinc–telluride gamma camera. *Sci Rep.* 2021;11:24320.
- [207] Tanaka K, Norikane T, Mitamura K, Yamamoto Y, Maeda Y, Fujimoto K, et al. Quantitative [^{99m}Tc]Tc-MDP SPECT/CT correlated with [¹⁸F]NaF PET/CT for bone metastases in patients with prostate cancer. *EJNMMI Phys.* 2022;9:83.
- [208] Phillips WT, Gorzell BC, Martinez RA, Salman UA, Cooper AW, Stocker DJ, et al. Fewer-angle SPECT/CT blood pool imaging for infection and inflammation. *J Nucl Med Technol.* 2021;49:39–43.
- [209] Phillips WT, Kukkar V, Francis GL, Gorzell BC, Cooper AW, Metter DF, et al. FASpecT/CT, a new SPECT/CT acquisition with higher sensitivity and efficiency in radioiodine thyroid cancer imaging. *Clin Nucl Med.* 2020;45:356–364.
- [210] Kakhki V, Anvari K, Sadeghi R, Mahmoudian AS, Torabian-Kakhki M. Pattern and distribution of bone metastases in common malignant tumors. *Nucl Med Rev.* 2013;16:66–69.
- [211] Roth D, Larsson E, Sundlöv A, Sjögreen Gleisner K. Characterisation of a hand-held CZT-based gamma camera for ¹⁷⁷Lu imaging. *EJNMMI Phys.* 2020;7:46.
- [212] Song H, Ferri V, Duan H, Aparici CM, Davidzon G, Franc BL, et al. SPECT at the speed of PET: a feasibility study of CZT-based whole-body SPECT/CT in the post ¹⁷⁷Lu-DOTATATE and ¹⁷⁷Lu-PSMA617 setting. *Eur J Nucl Med Mol Imaging.* 2023;50:2250–2257.
- [213] Visvikis D, Lambin P, Beuschau Mauridsen K, Hustinx R, Lassmann M, Rischpler C, et al. Application of artificial intelligence in nuclear medicine and molecular imaging: a review of current status and future perspectives for clinical translation. *Eur J Nucl Med Mol Imaging.* 2022;49:4452–4463.
- [214] Hustinx R, Pruijm J, Lassmann M, Visvikis D. An EANM position paper on the application of artificial intelligence in nuclear medicine. *Eur J Nucl Med Mol Imaging.* 2022;50:61–66.
- [215] Pan B, Qi N, Meng Q, Wang J, Peng S, Qi C, et al. Ultra high speed SPECT bone imaging enabled by a deep learning enhancement method: a proof of concept. *EJNMMI Phys.* 2022;9:43.
- [216] Qi N, Pan B, Meng Q, Yang Y, Feng T, Liu H, et al. Deep learning enhanced ultra-fast SPECT/CT bone scan in patients with suspected malignancy: quantitative assessment and clinical performance. *Phys Med Biol.* 2023;68:135012.
- [217] Zhao Z, Pi Y, Jiang L, Xiang Y, Wei J, Yang P, et al. Deep neural network based artificial intelligence assisted diagnosis of bone scintigraphy for cancer bone metastasis. *Sci Rep.* 2020;10:17046.
- [218] Lin Q, Li T, Cao C, Cao Y, Man Z, Wang H. Deep learning based automated diagnosis of bone metastases with SPECT thoracic bone images. *Sci Rep.* 2021;11:4223.
- [219] Aide N, Lasnon C, Veit-Haibach P, Sera T, Sattler B, Boellaard R. EANM/EARL harmonization strategies in PET quantification: from daily practice to multicentre oncological studies. *Eur J Nucl Med Mol Imaging.* 2017;44:17–31.



**TURUN
YLIOPISTO**
UNIVERSITY
OF TURKU

ISBN 978-951-29-9839-5 (PRINT)
ISBN 978-951-29-9840-1 (PDF)
ISSN 0355-9483 (Print)
ISSN 2343-3213 (Online)

